AGU PUBLICATIONS

Geochemistry, Geophysics, Geosystems

RESEARCH ARTICLE
10.1002/2016GC006545

Special Section:
FRONTIERS IN GEOSYSTEMS: Deep Earth - surface interactions

Cenozoic epeirogeny of the Indian peninsula

F. D. Richards[1], M. J. Hoggard[1], and N. J. White[1]

[1]Bullard Laboratories, Department of Earth Sciences, University of Cambridge, Cambridge, UK

Key Points:
- Oceanic residual depth anomalies show regional tilt of Indian Plate
- Calibrated inverse modeling of drainage networks suggests that this tilt grew in Neogene times
- Vertical motions can be linked to temperature anomalies within a sub-plate asthenospheric channel

Supporting Information:
- Supporting Information S1
- Data Set S1
- Table S1

Correspondence to:
F. D. Richards,
fdr22@cam.ac.uk

Citation:
Richards, F. D., M. J. Hoggard, and N. J. White (2016), Cenozoic epeirogeny of the Indian peninsula, *Geochem. Geophys. Geosyst.*, *17*, 4920–4954, doi:10.1002/2016GC006545.

Received 20 JUL 2016
Accepted 10 NOV 2016
Accepted article online 17 NOV 2016
Published online 22 DEC 2016

Abstract Peninsular India is a cratonic region with asymmetric relief manifest by eastward tilting from the 1.5 km high Western Ghats escarpment toward the floodplains of eastward-draining rivers. Oceanic residual depth measurements on either side of India show that this west-east asymmetry is broader scale, occurring over distances of $>$ 2000 km. Admittance analysis of free-air gravity and topography shows that the elastic thickness is 10 $\pm$ 3 km, suggesting that regional uplift is not solely caused by flexural loading. To investigate how Indian physiography is generated, we have jointly inverted 530 river profiles to determine rock uplift rate as a function of space and time. Key erosional parameters are calibrated using independent geologic constraints (e.g., emergent marine deposits, elevated paleosurfaces, uplifted lignite deposits). Our results suggest that regional tilt grew at rates of up to 0.1 mm a^{-1} between 25 Ma and the present day. Neogene uplift initiated in the south and propagated northward along the western margin. This calculated history is corroborated by low-temperature thermochronologic observations, by sedimentary flux of clastic deposits into the Krishna-Godavari delta, and by sequence stratigraphic architecture along adjacent rifted margins. Onset of regional uplift predates intensification of the Indian monsoon at 8 Ma, suggesting that rock uplift rather than climatic change is responsible for modern-day relief. A positive correlation between residual depth measurements and shear wave velocities beneath the lithosphere suggests that regional uplift is generated and maintained by temperature anomalies of $\pm$100 °C within a 200 $\pm$ 25 km thick asthenospheric channel.

1. Introduction

The physiography of peninsular India is characterized by eastward tilting and predominantly eastward-flowing drainage (Figure 1a) [*Powar*, 1993; *Collier et al*., 2008]. The age and origin of this asymmetric configuration is much debated. For example, it has been argued that the Western Ghats escarpment is a topographic relic of rifting and magmatism that developed at ~65 Ma along the Western Indian continental margin [*White and McKenzie*, 1989; *Cox*, 1989; *Pandey et al*., 1996]. Alternatively, it has been suggested that regional uplift is much younger with neotectonic activity playing an important role [*Valdiya*, 2001; *Vita-Finzi*, 2004]. With regard to mechanism, a flexural response to combined onshore denudation and offshore sedimentary loading has been invoked to account for elevation of the western coastline [*Watts and Cox*, 1989; *Whiting et al*., 1994; *Gunnell and Fleitout*, 1998; *Campanile et al*., 2008]. Regional epeirogenic uplift caused by thermal anomalies within the convecting mantle have also been proposed [*Kailasam*, 1975; *Radakrishna*, 1991]. These different suggestions make testable predictions about the temporal and spatial pattern of uplift and tilting that is currently poorly known.

Active tectonic deformation is unlikely to account for the present-day topographic tilt of the Indian peninsula. Background seismicity is modest and large magnitude (i.e., $M_b \geq 6$) earthquakes are relatively rare. Most of these events are located within Proterozoic mobile belts that are oblique to the axis of regional tilting [*Widdowson and Mitchell*, 1999; *Valdiya*, 2001; *Mishra et al*., 2004; *Veeraswamy and Raval*, 2005; *Copley et al*., 2014] (Figure 1c). Along the western seaboard, focal mechanism solutions are mostly extensional. Within the continental interior and along the eastern seaboard, strike-slip and shortening mechanisms predominate, consistent with north-south-directed compressional stress [*Yamato et al*., 2013; *Müller et al*., 2015].

Here, we investigate Indian epeirogeny by analyzing and combining three different data sets which bear upon this regional problem. First, we examine the age-depth relationship of oceanic lithosphere surrounding peninsular India. It is well known that there are significant positive and negative residual depth anomalies with respect to plate cooling models throughout the oceanic realm [*Winterbourne et al*., 2014; *Hoggard*

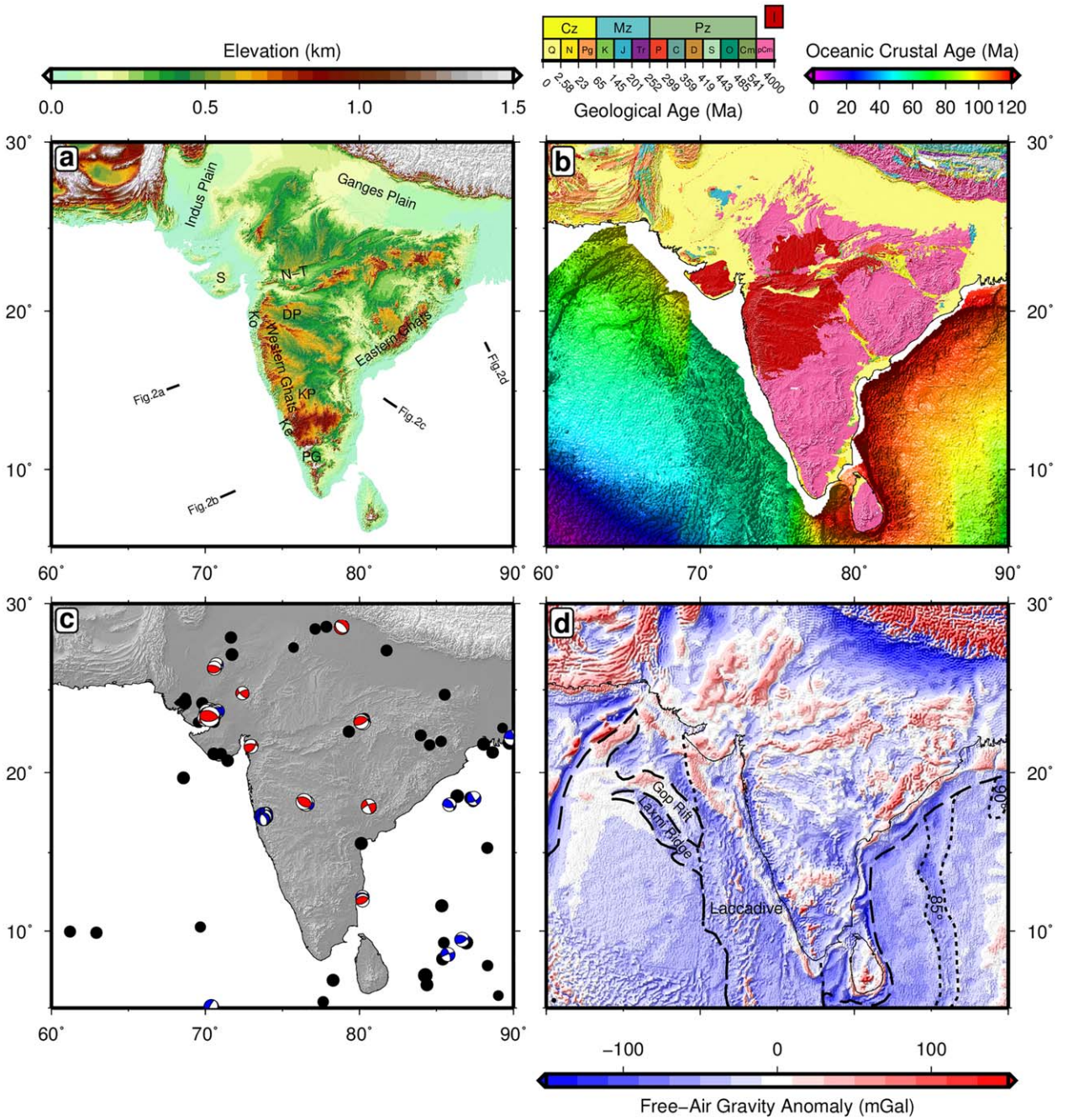

Figure 1. Indian topography, geology, active deformation, and free-air gravity anomalies. (a) Topographic map based on SRTM30_PLUS model [*Becker et al*., 2009]. DP = Deccan Plateau; Ke = Kerala Coastal Plain; Ko = Konkan Coastal Plain; KP = Karnataka Plateau; N-T = Narmada-Tapti Valley; S = Saurashtra Peninsula. Black lines = seismic profiles shown in Figure 2. (b) Simplified geologic map with oceanic crustal ages [*Wandrey and Law*, 1997; *Müller et al*., 2008]. (c) Intraplate earthquake seismicity. Black circles = earthquakes with $M_b \geq 3$ for 1964–2015 taken from International Seismological Center EHB catalog [*Engdahl et al*., 1998]; blue beach balls = focal mechanisms from Centroid Moment Tensor catalog (www.globalcmt.org); scaled red beach balls = focal mechanisms according to magnitude calculated by inverse modeling of body waveforms from *Copley et al*. [2014]. (d) Free-air gravity anomaly map [*Sandwell et al*., 2014]. Dashed lines = continent-ocean boundary; dotted lines = volcanic tracks including Laccadive, 85 °E and 90 °E ridges.

et al., 2016]. These anomalies typically have water-loaded amplitudes of $\pm 10^2$–10^3 m and wavelengths of 10^2-10^3 km. By measuring the distribution of these anomalies on either side of India, it is possible to frame the epeirogenic consequences for the peninsula itself. We are especially interested in the way in which offshore bathymetric anomalies may be expressed within the adjacent continental topography. Second, we create a digital database of longitudinal river profiles that drain the subcontinent. This drainage inventory is

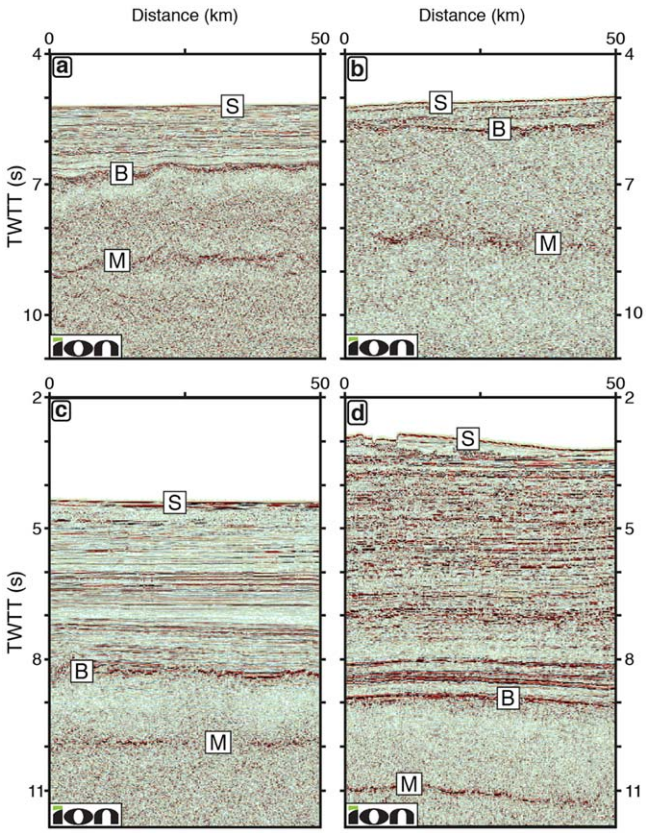

Figure 2. Portions of seismic reflection profiles used to calculate residual depth anomalies of oceanic lithosphere (Figure 1a). (a) 60 Ma oceanic crust located south-west of Mumbai. S = seabed; B = sediment-basement interface; M = Moho. Crustal age from magnetic anomalies [*Müller et al*., 2008]. (b) 54 Ma oceanic crust located west of Kerala. (c) 115 Ma oceanic crust located south of Krishna-Godavari delta. (d) 110 Ma oceanic crust beneath southern Bengal Fan. Images shown courtesy of ION Geophysical Corporation.

inverted using a stream-power formulation to determine the spatial and temporal pattern of regional rock uplift subject to independent geologic calibration and testing. Third, we investigate the relationship between these observations and the distribution of seismic velocity anomalies from tomographic models. Our principal goal is to show how disparate offshore, onshore, and sub-plate observations can be combined to generate an improved quantitative understanding of the timing and causes of Indian epeirogeny.

2. Regional Framework

2.1. Residual Depth Measurements

The Indian subcontinent is bounded to the east and west by Cretaceous and Paleogene oceanic lithosphere, respectively (Figure 1b). It is well known that significant residual depth anomalies occur in the oceanic realm and that these anomalies are a useful guide for determining the spatial pattern of dynamic topography adjacent to continental margins [*Czarnota et al*., 2013; *Hoggard et al*., 2016]. We have carried out age-depth analysis of a database of regional seismic reflection images generously provided by ION Geophysical Corporation (Figures 1a and 2). On each of these images, the sedimentary pile overlying *bona fide* oceanic crust together with the base of the crust are clearly visible. We have used these observations to accurately calculate the water-loaded depth to basement following the methodology of *Hoggard et al*. [2016]. During this analysis, considerable care was taken to avoid areas where crustal flexure was evident or where the presence of oceanic crust is ambiguous [*Todal and Edholm*, 1999; *Chaubey et al*., 2002] (Figures 1d and 2).

On each image, residual depth anomalies are calculated by measuring the difference between water-loaded subsidence of the top of oceanic basement and an assumed age-depth relationship. We exploit the age-depth compilation of *Crosby and McKenzie* [2009] since their approach attempts to specifically exclude regions where dynamic topographic support is significant, as inferred from the magnitude of long-wavelength ($\lambda \geq 3000$ km) gravity anomalies. Note that the size and polarity of these residual depth anomaly measurements are not significantly affected if a large range of alternative age-depth models are used [e.g., *Hoggard et al*. 2016] (Figure 3a).

Our results show that there is a marked difference in residual depth anomalies on either side of India. To the west, Paleogene oceanic crust is up to 1 km shallower than expected. To the east, Cretaceous oceanic crust is up to 1.2 km deeper than expected. It is important to emphasize that these water-loaded anomalies are not caused by differences in the thickness of either sediment or crust whose effects have been carefully removed. Instead, they reflect the presence of regional negative and positive density anomalies either within the lithospheric mantle, the sublithospheric mantle, or both. Figure 3b shows the spatial distribution of these residual depth anomalies. West of India, amplitudes of positive residual depth anomalies decrease slightly from east to west away from the coastline but there is little evidence for a north-south gradient.

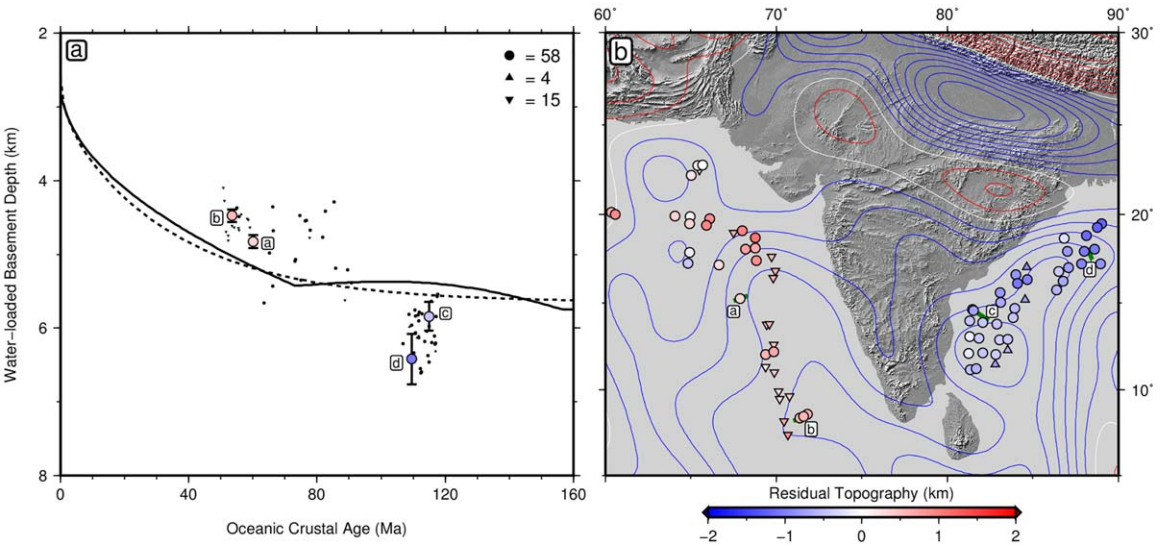

Figure 3. Residual depth anomalies of oceanic crust. (a) Water-loaded subsidence of oceanic lithosphere as function of age. Solid line = age-depth relationship of *Crosby and McKenzie* [2009]; dotted line = age-depth relationship of *Stein and Stein* [1992]; solid circles/triangles = age-depth measurements averaged in 1° bins; red/blue circles with vertical bars = age-depth measurements and uncertainties calculated from seismic profiles shown in Figure 2. (b) Red/blue circles and upward/downward-pointing triangles = positive/negative residual depth anomaly measurements and upper/lower bounds; red/blue contours = positive/negative long-wavelength (> 730 km) free-air gravity anomalies at 10 mGal intervals calculated from GGM03 data set [*Tapley et al.*, 2007]; labeled green lines = location of seismic profiles shown in Figure 2.

East of India, amplitudes of negative anomalies increase steadily from south to north. These results build upon previously published estimates that only corrected for sedimentary loading [*Ajay and Chaubey*, 2008].

Given the assumed compositional homogeneity of oceanic lithosphere, these residual depth anomalies are probably maintained by density variations that occur within the sublithospheric mantle since their size would require what are currently regarded as implausibly large variations in mantle composition [*Dalton et al.*, 2014]. Elsewhere, a good correlation between long-wavelength (700–9000 km) free-air gravity anomalies and residual depth measurements has been observed [*Winterbourne et al.*, 2014; *Hoggard et al.*, 2016]. No such correlation is observed here where negative long-wavelength gravity anomalies predominate, consistent with the existence of a significant (∼100 m) geoid low [*Kaula*, 1963; *Bruinsma et al.*, 2014]. This lack of correlation between geoid and surface deflection implies that the positive mass anomaly that generates and maintains the geoid low is deep-seated [*Hager et al.*, 1985; *Colli et al.*, 2016; *Nerlich et al.*, 2016].

The offshore pattern of residual depth anomalies mirrors the onshore asymmetry of topographic relief (Figure 4). Peninsular India is dominated by a long-wavelength eastward tilt from the Western Ghats escarpment, where average elevation is ∼1.5 km, down to the alluvial floodplains along the east coast. This pattern of relief is matched by a strongly asymmetric drainage configuration whereby rivers with headwaters positioned < 50 km from the Arabian Sea drain into the Bay of Bengal, more than 500 km to the east. The close match between the polarity and gradient of regional tilting either side of, and across, India is striking (Figure 4). The wavelength of ∼2000 km and amplitude of ±1 km, coupled with its continuity across both oceanic and continental lithosphere, is suggestive of an underlying, sub-plate mechanism [*Panasyuk and Hager*, 2000]. Offshore, it is difficult to determine the temporal evolution of residual depth anomalies. In contrast, the growth of onshore regional topography can, in principle, be determined by combined studies of stratigraphic, geomorphic, and thermochronologic observations. In order to place this approach in context, we first examine the large-scale structure of the crust and lithosphere.

2.2. Crustal and Lithospheric Isostasy

The continental realm contains indirect information about the temporal evolution of regional topography. However, determining continental residual topography is less straightforward since the density and thickness of heterogeneous crust and lithospheric mantle are relatively poorly known. An appropriate starting point is a database of crustal thickness measurements assembled from a combination of seismic refraction experiments and receiver function analyses [*Kaila*, 1979; *Kaila et al.*, 1981; *Saul et al.*, 2000; *Ravi Kumar et al.*,

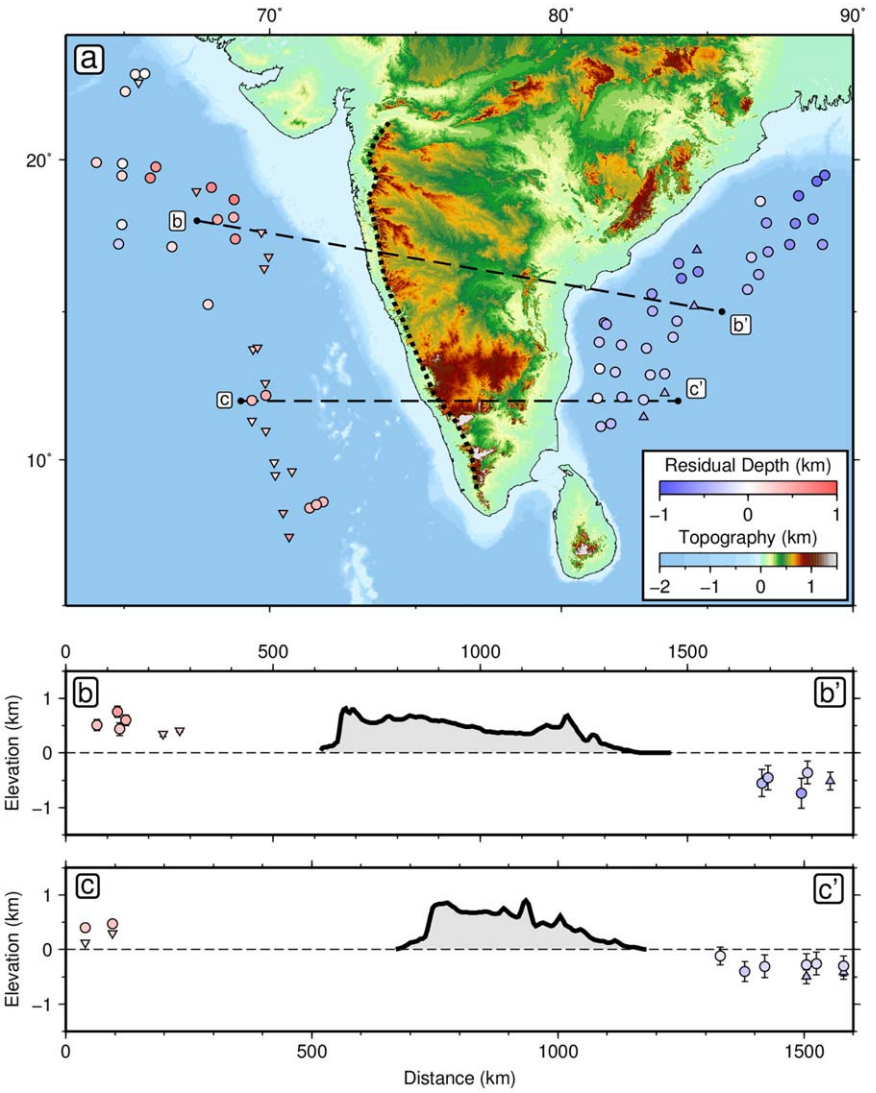

Figure 4. Air-loaded residual depths and onshore topography. (a) Topographic and bathymetric map from SRTM30_PLUS model [*Becker et al.* 2009]. Red/blue circles and upward/downward-pointing triangles = air-loaded residual depth anomaly measurements and upper/lower bounds; dashed lines labeled b–b′ and c–c′ = location of transects shown in Figures 4b and 4c. (b) Northern transect showing offshore air-loaded residual depth anomalies and onshore topographic profile. Solid line = low-pass filtered topography (Gaussian function with 25 km moving window); horizontal dashed line = reference level. (c) Southern transect.

2001; *Sarkar et al.*, 2003; *Gupta et al.*, 2003; *Reddy*, 2005; *Tiwari et al.*, 2006; *Jagadeesh and Rai*, 2008; *Mitra et al.*, 2008; *Julià et al.*, 2009; *Acton et al.*, 2011; *Behera*, 2011; *Kayal et al.*, 2011; *Mandal*, 2012; *Borah et al.*, 2014; *Praveen Kumar and Mohan*, 2014; *Singh et al.*, 2015] (Figure 5; Supporting Information S1; Data Set S1). Bulk *P* wave velocities are 6.23–6.89 km s^{-1} which yield average crustal densities of 2.76–2.9 Mg m^{-3}, according to empirical velocity-density relationships [*Brocher*, 2005; *Maceira and Ammon*, 2009].

An isostatic model can be used to predict elevation from these crustal thicknesses and densities. Observed elevations deviate substantially from this Airy isostatic relationship which implies that some fraction of elevation is maintained by other means [*Rai et al.*, 2013] (Figure 5). The narrow range of crustal density variation combined with an absence of an east-west trend suggest that observed isostatic deviations are not easily accounted for by crustal heterogeneity. In particular, there is little evidence for magmatic underplating along the Western Ghats south of 20 °N where the highest average elevation occurs [*Tiwari et al.*, 2006; *Rao et al.*, 2015]. Instead, it is more likely that subcrustal heterogeneity plays an important role in generating and maintaining some proportion of Indian topography.

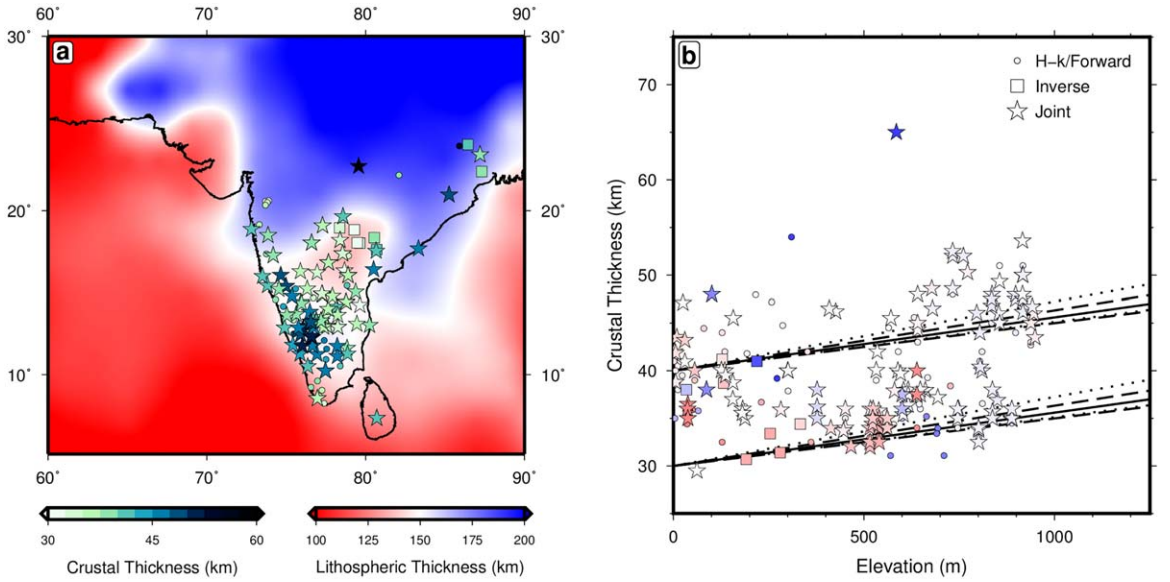

Figure 5. Crustal isostasy and lithospheric thickness. (a) Lithospheric thickness based upon surface wave tomographic model. Symbols are published crustal thickness estimates [*Priestley and McKenzie*, 2013] (Supporting Information Data Set S1). Stars = crustal thicknesses calculated by joint inversion of receiver functions and surface wave dispersion curves [e.g., *Rai*, 2003; *Julià et al.*, 2009; *Rai et al.*, 2009; *Acton et al.*, 2010, 2011; *Vijay Kumar et al.*, 2012; *Mandal*, 2012; *Borah et al.*, 2014]; squares = crustal thicknesses from inverse modeling of receiver functions [e.g., *Mitra et al.*, 2008; *Kayal et al.*, 2011; *Singh et al.*, 2012; *Praveen Kumar and Mohan*, 2014]; dots = crustal thicknesses calculated by either forward modeling or *H-k* stacks of receiver functions [e.g., *Saul et al.*, 2000; *Ravi Kumar et al.*, 2001; *Gupta et al.*, 2003; *Rai et al.*, 2005; *Pathak et al.*, 2006; *Tiwari et al.*, 2006; *Jagadeesh and Rai*, 2008; *Rai et al.*, 2013]. (b) Crustal thickness plotted as function of elevation for different lithospheric thicknesses. Colored stars/squares/dots = crustal thicknesses calculated as before where color indicates lithospheric thickness at that location; solid lines = isostatic relationships determined by equalizing lithostatic pressure at base of either 30 or 40 km thick crust using crustal density of 2.7 Mg m^{-3}; dashed lines = relationships calculated for crustal densities of 2.65 and 2.75 Mg m^{-3}; dotted lines = relationships calculated for crustal densities of 2.76 and 2.9 Mg m^{-3} (i.e., density range estimated from v_p/v_s ratios) [*Brocher*, 2005].

Although much of northern India is dominated by thick (> 150 km) lithosphere, there is evidence that continental lithosphere as thin as 100 km lies beneath the southwestern portion of the peninsula [*N. Kumar et al.*, 2013; *P. Kumar et al.*, 2013; *Priestley and McKenzie*, 2013]. This variation in lithospheric thickness could play a role in supporting the elevation of the Western Ghats. However, the relationship between crustal thickness, lithospheric thickness, and regional elevation is not consistent with a straightforward isostatic balance which implies that a component of sub-plate support may be required.

2.3. Flexural Analysis

The spectral relationship between free-air gravity anomalies and topography is analyzed to determine the flexural rigidity of the Indian plate [*Becker et al.*, 2009; *Förste et al.*, 2011]. First, the admittance, $Z(k)$, which is the ratio of free-air gravity and topographic anomalies as a function of wave number, k, is calculated within a 1550 × 1950 km^2 box that encompasses the bulk of peninsular India (Figures 6a and 6b). Z is a measure of the degree of compensation and is often used to determine T_e, the elastic thickness. At short-wavelengths, Z approaches a constant value of ~120 mGal km^{-1}. Using the infinite slab approximation, $Z \sim 2\pi\rho_{cu}G$ where G=6.67×10^{-11} m^3 kg^{-1} s^{-2} [*Watts*, 2001]. This approximation yields an upper crustal density of $\rho_{cu} \sim 2.9$ Mg m^{-3}. It is consistent with estimates of crustal density obtained from receiver function studies and reflects the fact that basaltic rocks and Precambrian basement of amphibolite-granulite facies are the predominant lithologies [*Newton and Hansen*, 1986].

An inverse model is used to calculate T_e and to estimate the percentage of subsurface loading [*McKenzie and Fairhead*, 1997; *McKenzie*, 2003]. This model seeks a value of T_e that minimizes the misfit between observed and calculated values of Z (Figures 6c and 6d). We obtain a T_e of $9.8^{+3.7}_{-2.0}$ km with a subsurface loading percentage of 17^{+27}_{-13}%. This value agrees with that of *McKenzie et al.* [2015] who analyzed a smaller box located in the northern half of the box used here. It is also consistent with the average regional value obtained by coherency analysis of Bouguer gravity anomalies by *Mouthereau et al.* [2013]. We note in passing that admittance and Bouguer coherency studies yield similar values of T_e provided that large topographic signals exist, which are at least partially coherent with the free-air gravity field [*McKenzie*, 2016].

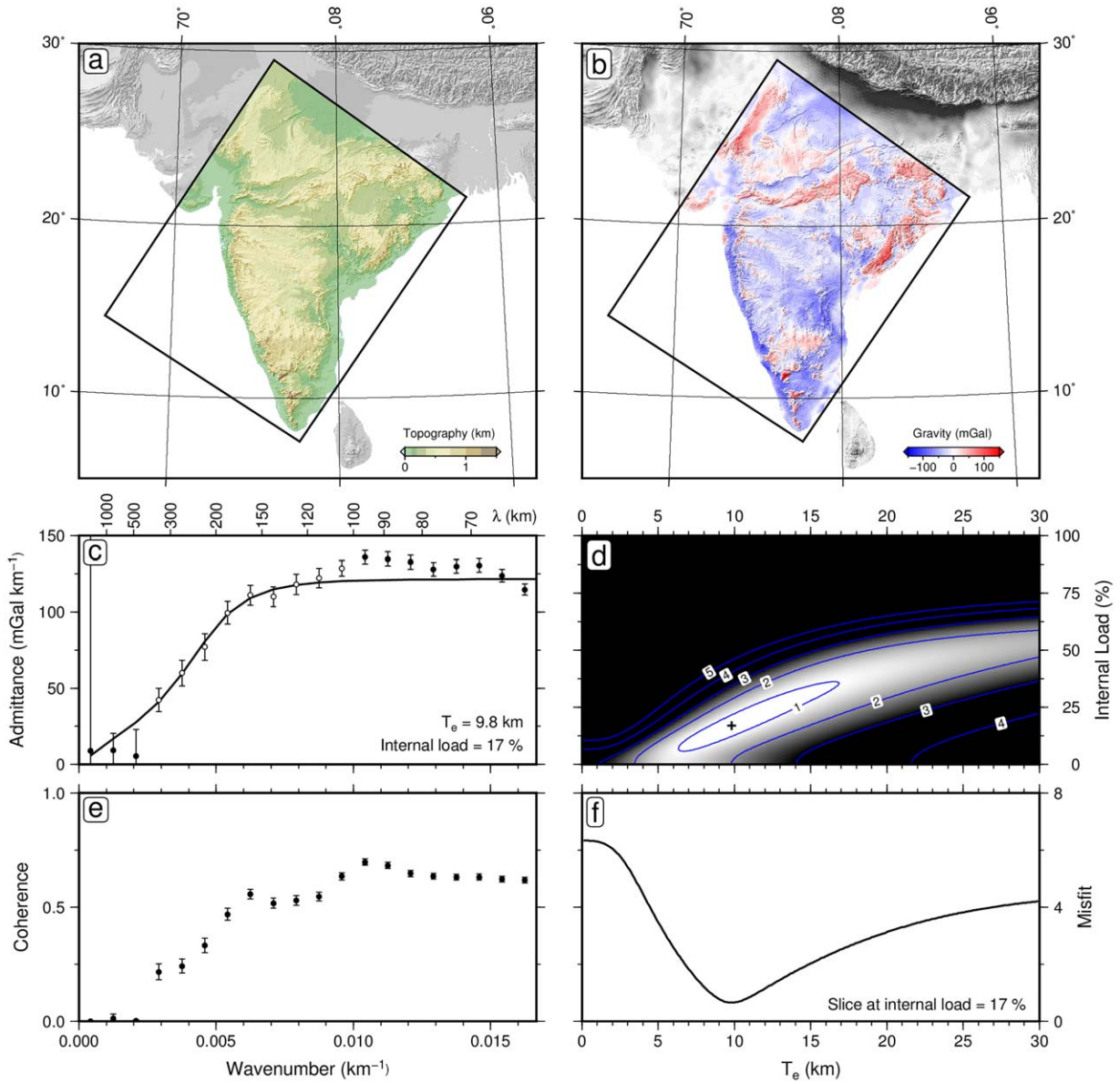

Figure 6. Admittance analysis of gravity and topography. (a) Map of topography based upon SRTM30_PLUS model [*Becker et al.*, 2009]. Oblique box = region of analysis (1550 × 1950 km ^{2}). (b) Map of free-air gravity anomalies calculated from EIGEN-6C3stat data set at 6 min resolution [*Förste et al.*, 2011]. (c) Open/solid circles with vertical bars = observed admittance values with $\pm 1\sigma$ plotted as function of wave number; solid line = theoretical admittance function that best fits open circles (100 km $\leq \lambda \leq$ 400 km) calculated for elastic plate model where T_e = 9.8 km, internal load = 17%, crustal thickness = 35 km, upper crustal thickness = 15 km, upper crustal density = 2.9 Mg m^{-3}, lower crustal density = 2.95 Mg m^{-3}. (d) RMS misfit between observed and calculated admittance plotted as function of T_e and internal load. Black cross = locus of global minimum. (e) Coherence between free-air gravity anomaly and topography plotted as function of wave number. (f) Slice through misfit function shown in Figure 6d for internal load of 17%. Doubling of minimum misfit value yields T_e range of 7.8–12.5 km.

The value of T_e determines the wavelength over which flexural deformation can be supported [*Watts*, 2001]. This wavelength is approximately $\pi\alpha$ where

$$\alpha = \left[\frac{(\rho_m - \rho_s)g}{4D}\right]^{-1/4}, \tag{1}$$

and

$$D = \frac{ET_e^3}{12(1-\nu^2)}. \tag{2}$$

ρ_m = 3.3 Mg m^{-3} is mantle density, ρ_s = 2.0 Mg m^{-3} is the density of infilling sedimentary rocks, g = 9.81 m s^{-2}, $E = 10^{11}$ N m^{-2} is Young's modulus, and ν = 0.25 is Poisson's ratio. Substitution yields a $\pi\alpha$

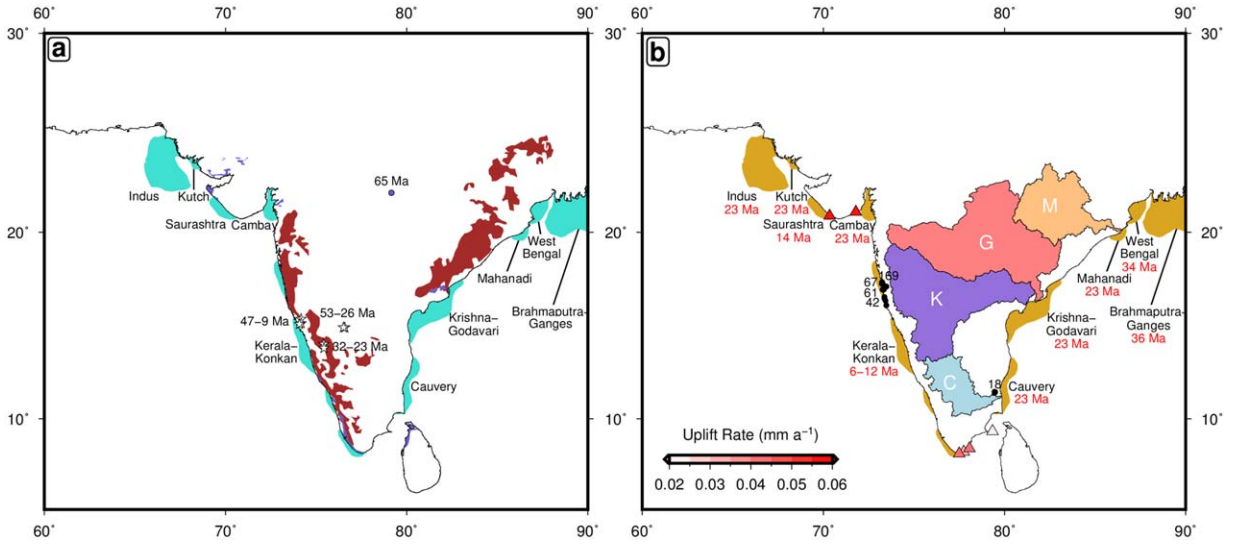

Figure 7. Cenozoic paleogeography. (a) Summary of Eocene-Oligocene paleogeography. Red polygons = lateritic deposits [*FAO-UNESCO*, 2007]; labeled stars = locations and ages of laterites dated by $^{40}Ar/^{39}Ar$ analysis of cryptomelane [*Bonnet et al*., 2016]; blue circle = Early Paleocene (64.8 Ma) marine deposits [*Keller et al*., 2009]; blue polygons = Miocene marine deposits [*Wandrey and Law*, 1997]; turquoise polygons = carbonate-dominated deltaic sedimentary deposits [*Raju*, 2008]. (b) Miocene-Recent paleogeography. Orange/red/purple/blue polygons = Mahanadi/Godavari/Krishna/Cauvery drainage catchments; labeled yellow polygons = clastic-dominated deltaic sedimentary deposits (number in red = age of transition from carbonate to clastic-dominated deposition) [*Raju*, 2008]; colored triangles = elevated Pleistocene marine terraces with uplift rate given by color-scale bar [*Pedoja et al*., 2011]; labeled black circles = Mio-Pliocene lignite deposits with elevations in meters [*Brückner*, 1987; *Singh et al*., 1992; *Suryawanshi and Golekar*, 2014].

of 126^{+28}_{-19} km. This value is significantly smaller than the >2000 km wavelength of regional tilting and suggests that regional epeirogeny is not exclusively generated and maintained by flexural processes.

At the very longest wavelengths, the coherence between the free-air gravity field and topography tends to zero. This lack of coherence directly arises from the anticorrelation between negative long-wavelength free-air gravity anomalies and positive topographic tilting (Figure 3b).

3. Drainage Analysis

Indian physiography is markedly asymmetric (Figure 1a). This asymmetry dominates many aspects of its geomorphology including the drainage network. In principle, ubiquitous drainage networks should preserve coherent signals of temporally and spatially varying rock uplift rates [*Whipple*, 2009]. *Pritchard et al*. [2009] and *Roberts and White* [2010] have shown that longitudinal river profiles can be inverted as a function of regional uplift subject to independent geologic calibration.

Cox [1989] argued that the present-day topography and drainage of India was created during Paleogene times when the Seychelles rifted away from the western margin in the presence of a mantle plume. However, there is increasing evidence that any elevated topography generated during Deccan volcanism was rapidly eroded away and that relief was negligible by the beginning of Neogene times. During Eocene and Oligocene times, widespread lateritic deposits developed inboard of both margins [*Bonnet et al*., 2014, 2016] (Figure 7a). Combined with additional paleoclimatic observations, this lateritization suggests that a wet, tropical climate with low relief prevailed across most of peninsular India at this time [*Kent and Muttoni*, 2008; *Thorne et al*., 2012; *Chatterjee et al*., 2013]. Offshore, the Kerala-Konkan, Mahanadi, Krishna-Godavari, and Cauvery deltas were dominated by fringing carbonate reef complexes, which suggests that the flux of clastic sediment was modest, despite humid climatic conditions. This observation provides further evidence for limited topographic relief within drainage catchments during this period [*Raju*, 2008].

Between Miocene times and the present day, these deltas have evidently experienced major influxes of clastic material that rapidly prograded at adjacent continental shelves (Figure 7b). The dramatic change in paleogeography suggests that the present-day topography is relatively youthful. An important corollary is that the drainage network probably contains useful information about the spatial and temporal distribution

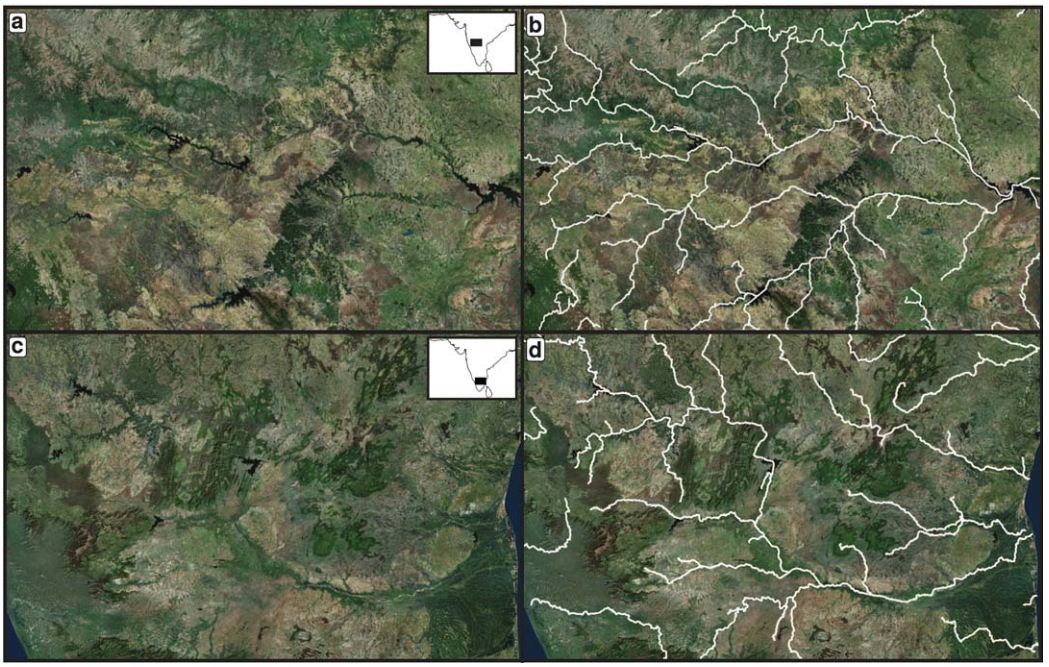

Figure 8. Landsat images of drainage patterns. (a) Map showing Landsat image of portion of southern Deccan Plateau (see inset map). (b) Landsat image overlain by drainage pattern recovered from flow-routing algorithms. (c) Map showing Landsat image of portion of southern Karnataka and Palghat Gap region (see inset map). (d) Landsat image overlain by recovered drainage pattern.

of topographic growth. Circumstantial evidence for modest pre-Neogene topographic relief suggests that it is reasonable to prescribe a flat, zero elevation, starting condition for inverse modeling of drainage networks. We emphasize that any starting condition could be used for inverse modeling and that inclusion of moderate topographic relief would be unlikely to dramatically alter our principal conclusions. A combination of stratigraphic relationships, incision patterns, and the great distances over which Paleocene lavas flowed, imply that eastward-directed drainage patterns were established by this time [*Cox*, 1989; *Knight et al*., 2003; *Sheth*, 2007]. Deep incision of the Eastern Ghats region by eastward-flowing rivers provides corroborative evidence that these drainage patterns are probably antecedent and have therefore been relatively stable over a long period [*Widdowson and Cox*, 1996; *Gunnell and Harbor*, 2010].

3.1. Drainage Inventory

A digital elevation model was compiled using the Advanced Spaceborne Thermal Emission and Reflection Radiometer (ASTER) data set, which was decimated to yield a pixel size of 60 m. Vertical resolution is 17 m at the 95% confidence level [*Meyer et al*., 2011]. First, anomalous spikes and sinks were removed using ArcGIS hydrologic tools. Drainage networks were then recreated using standard flow-routing algorithms. Overland flow is set to occur when upstream drainage area exceeds 15 km^2, which is reasonable for a valley slope of intermediate gradient [*Montgomery and Dietrich*, 1988].

A total of 1916 longitudinal river profiles were extracted, from which a smaller peninsular inventory of 530 rivers was selected. This smaller data set specifically excludes the Narmada and Tapti basins where Cenozoic faulting may have modified or even reversed local drainage planforms [*Tarboton*, 1997; *Copley et al*., 2014]. In areas where there is negligible topography and/or internal drainage, the ability to adequately recover drainage networks can be compromised and the effective horizontal resolution decreases to hundreds of meters. In all regions, fidelity of the recovered drainage pattern was carefully checked using Landsat imagery (Figure 8). Extracted rivers that deviated significantly from their true courses were excised. In general, drainage recovery is excellent across peninsular India.

A useful by-product of drainage extraction is the landscape response time, τ_G, which records the potential length of the "tape recorder" that the drainage network represents [*Roberts et al*., 2012] (Figure 9). Note that strictly speaking, τ_G only applies within river channels. The maximum value of τ_G for India is 80 Ma which suggests that the peninsula-wide drainage pattern has the potential to record Cenozoic rock uplift history.

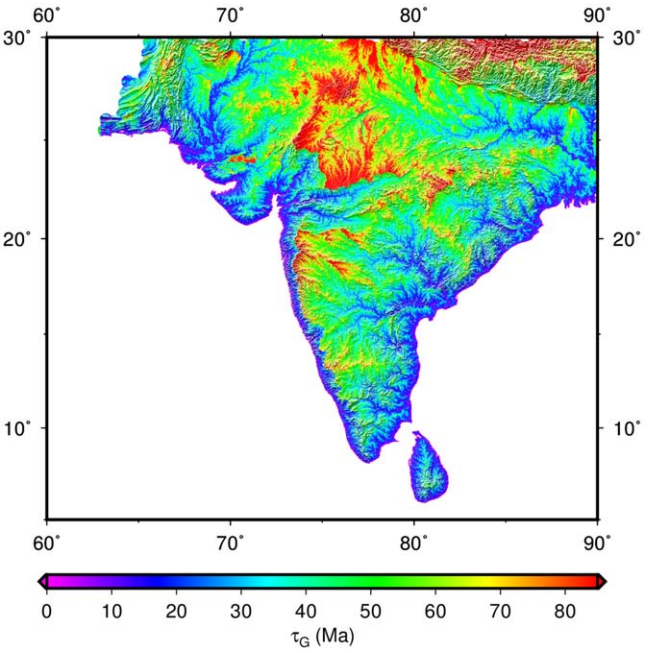

Figure 9. Landscape response time. Map of landscape response time, τ_G, calculated by solving equation (11) for each drainage catchment where $v = 3.7\ m^{0.26}\ Ma^{-1}$ and $m = 0.37$. Note that, strictly speaking, τ_G only applies within river channels.

τ_G was calculated by assuming that $v = 3.7$ and $m = 0.37$. These values were chosen by an independent calibration procedure that is described below. Within the Western Ghats, there is a marked disparity in τ_G at the drainage divide that separates rivers draining into the Arabian Sea from those draining into the Bay of Bengal.

It has been proposed that disparities in τ_G (or its dimensionless equivalent χ) at drainage divides are indicative of migration of the divide toward the catchment with a longer response time [*Willett et al.*, 2014]. Landscape response time assumes that rock uplift signals are inserted at river mouths and propagate upstream. In many regions such as India, Australia and North America, regional uplift has a spatially asymmetric distribution which means that rock uplift signals have been inserted at positions other than coastlines. Consequently, the juxtaposition of markedly different values of τ_G on either side of a drainage divide probably reflects the way in which the drainage networks are arranged with respect to the pattern of regional uplift. At the head of a given river, $A \rightarrow 0$ and $\tau_G \rightarrow \infty$ which means that the magnitude of any actual disparity in τ_G is also dependent upon the chosen overland flow threshold [*Willett et al.*, 2014; *Rudge et al.*, 2015]. Provided that the planform of uplift rate changes slowly, we suggest that drainage divides are quite likely to self-sharpen and lose elevation by landslide processes, ultimately giving rise to isolated erosional remnants.

From a practical perspective, the Western Ghats escarpment—despite having an apparently pronounced cross-divide disparity in τ_G—can only have retreated by $\leq$ 100 km since India-Seychelles rifting. This upper limit is the maximum distance between the continental shelf break and the present-day escarpment [*Gunnell*, 1997; *Widdowson and Mitchell*, 1999; *Kale and Subbarao*, 2004] (Figure 9). Lack of significant retreat implies that there has been a negligible change in upstream drainage area of the principal catchments. In the stream power formulation, upstream drainage area is taken to a fractional power which means that it can vary by $\pm$50% without significantly changing regional uplift histories determined by inverse modeling [*Paul et al.*, 2014]. This inference implies that changes in upstream drainage area triggered by drainage capture may not necessarily invalidate an inverse modeling strategy. Nevertheless, capture events could create knickzones that are not explicitly generated by regional uplift. Such knickzones probably occur close to watersheds and should be incoherent in space and time. If so, significant misfit excursions between observed and calculated rivers in affected catchments may be diagnostic of drainage capture. Thus, a range of geologic observations justify the simplifying assumptions used in inverse modeling of drainage networks, particularly the significant assumptions that the initial topography at $\sim$50 Ma had minimal relief and that the drainage planform has remained largely invariant.

In India, the recovered drainage network is dominated by four major river catchments: Mahanadi, Godavari, Krishna, and Cauvery (Figure 10). Three of these rivers, together with their major tributaries, rise along the Western Ghats or Sahyadri escarpment and drain into the Bay of Bengal. The Mahanadi river originates in the foothills of the Eastern Ghats, also known as Mahendra Parvatam.

Longitudinal river profiles for each of these four catchments are shown in Figures 10b–10e. Most of these river profiles have prominent long-wavelength knickzones that are indicative of disequilibrium. These knickzones have wavelengths of up to 300 km with amplitudes that consistently exceed 150 m. These wavelengths and amplitudes exceed changes in base level that are attributable to glacioeustatic sea-level

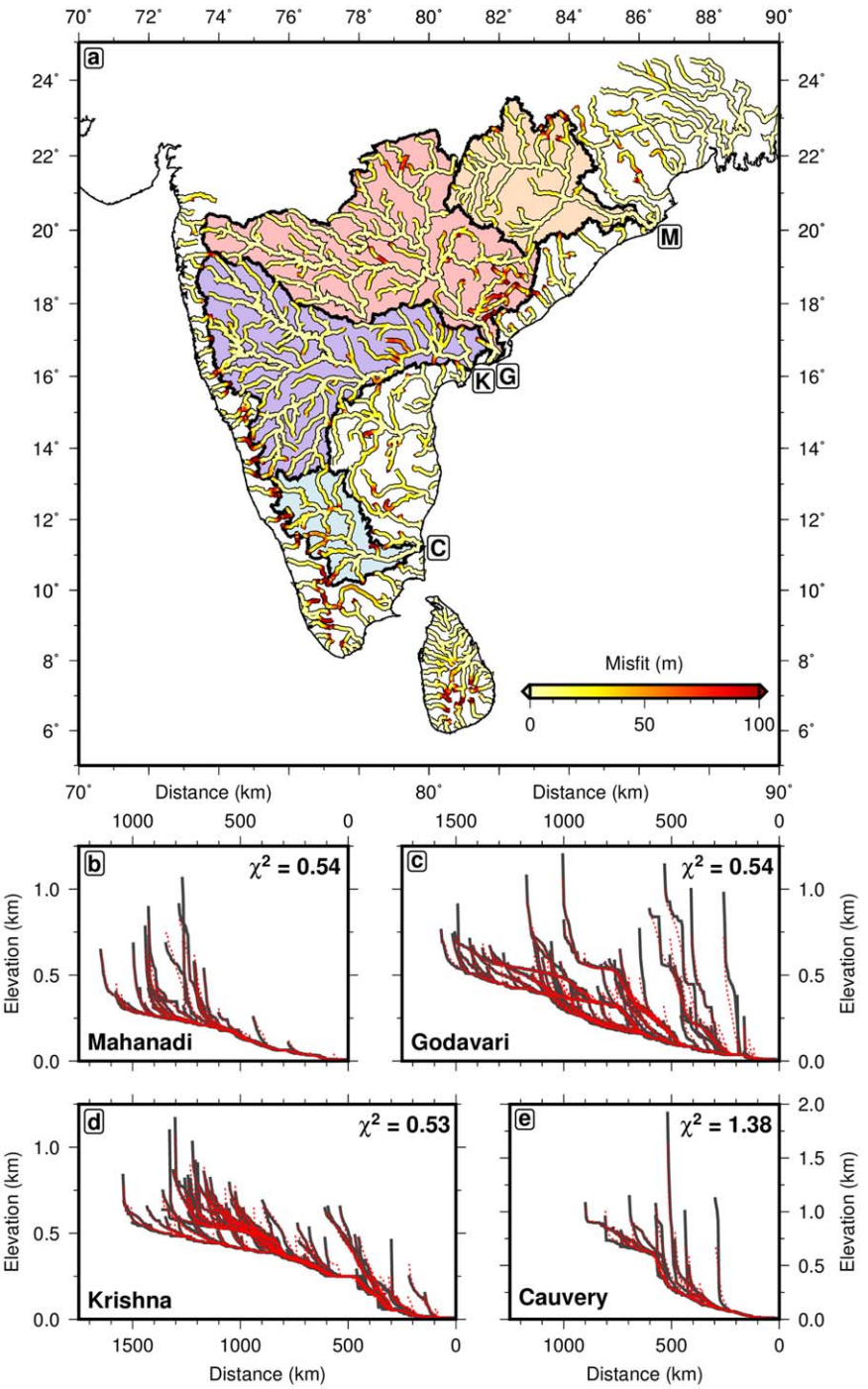

Figure 10. Observed and calculated river profiles. (a) Map showing extent of four largest drainage catchments and residual misfit between observed and calculated river profiles ($v = 3.7\ m^{0.26}\ Ma^{-1}$, $m = 0.37$, $\lambda_S = \lambda_T = 1$). Labels M/G/K/C = Mahanadi/Godavari/Krishna/Cauvery catchments; color scale = size of residual misfit in meters. (b) Godavari catchment. Black lines = observed river profiles; red dotted lines = calculated river profiles obtained by inverse modeling. Residual misfit shown in top right-hand corner. (c) Mahanadi catchment. (d) Krishna catchment. (e) Cauvery catchment.

fluctuations [*Siddall et al*., 2003; *Miller et al*., 2005]. There is poor correlation between major changes in lithology and knickzone development, indeed the majority of knickzones occur within the relatively homogeneous Precambrian basement or Deccan basalt of the cratonic interior [*Ambili and Narayana*, 2014; *Mandal et al*., 2016]. Furthermore, major knickzones do not coincide with the location of Archaean and Proterozoic fault systems, pointing to limited Cenozoic tectonic reactivation of these ancient structures [*Gunnell and*

Harbor, 2008; *Kale et al*., 2014]. The challenge is to exploit these sets of river profiles to constrain the spatial and temporal pattern of uplift rate for Cenozoic times.

3.2. Inverse Modeling

Change in elevation, z, as a function of time, t, along a longitudinal river profile depends upon the balance between the rate of regional rock uplift, $U(x, t)$, and the rate of erosion, $E(x, t)$, where x is distance along the profile. Thus

$$\frac{-\partial z}{\partial t} = E(x,t) + U(x,t). \tag{3}$$

The fluvial geomorphic community is primarily interested in developing a quantitative understanding of erosional processes. Here, we are interested in using river profiles to determine U, which means that $E(x, t)$ must be parameterized. It is usually assumed that E can be written in accordance with a stream power formulation such that

$$E(x,t) = -vA(x)^m \left(\frac{\partial z}{\partial x}\right)^n + \kappa \frac{\partial^2 z}{\partial x^2}, \tag{4}$$

where v is a calibration constant with the dimensions of velocity if $m = 0$, $A(x)$ is the upstream drainage area along a river profile, m and n are the concavity indices, and κ represents erosional "diffusivity." The first term on the right-hand side of equation (4) is advective and represents detachment-limited or "backwearing" processes. In other words, it determines the velocity at which knickzones migrate toward the head of a river [*Howard and Kerby*, 1983; *Whipple and Tucker*, 1999]. The second term is diffusive and represents transport-limited or "downwearing" processes [*Sklar and Dietrich*, 1998; *Sklar*, 2001; *Whipple*, 2002; *Tomkin*, 2003].

Previous studies show that the non-linear inverse problem can be posed and solved [*Roberts and White*, 2010; *Roberts et al*., 2012]. Inverse modeling of large inventories of river profiles suggests that equation (4) can be simplified in several important respects. First, river profiles are usually sampled every 5 km, yielding a minimum resolvable κ of $\sim 5 \times 10^6$ m^2 Ma^{-1}. This value is significantly greater than reported estimates which indicate that the diffusive term can be safely ignored [*Rosenbloom and Anderson*, 1994]. Second, *Paul et al*. [2014] and *Czarnota et al*. [2014] showed that the residual misfit between observed and calculated river profiles has a global minimum at $n = 1$, regardless of the degree of model regularization and smoothing. We acknowledge that this controversial result is not universally accepted but there is limited evidence from field studies that $n \sim 1$ [*Whittaker et al*., 2007; *Whittaker and Boulton*, 2012]. Furthermore, at the length scales of $10^2 - 10^3$ km considered here, there is no convincing evidence for shockwave behavior [*Pritchard et al*., 2009].

In the light of these earlier studies, we can write

$$\frac{-\partial z}{\partial t} = -vA^m \frac{\partial z}{\partial x} + U \tag{5}$$

This equation can be solved using the method of characteristic curves [*Luke*, 1972, 1974, 1976; *Weissel and Seidl*, 1998; *Pritchard et al*., 2009; *Goren et al*., 2014; *Rudge et al*., 2015]. The solution is written in the form $z(x,t) = z(x(t),t)$ since

$$\frac{\mathrm{d}z}{\mathrm{d}t} = \frac{\partial z}{\partial t} + \frac{\mathrm{d}x}{\mathrm{d}t}\frac{\partial z}{\partial x} = \left(vA^m + \frac{\mathrm{d}x}{\mathrm{d}t}\right)\frac{\partial z}{\partial x} - U(x(t),t). \tag{6}$$

which is expressed as two ordinary differential equations

$$\frac{\mathrm{d}x}{\mathrm{d}t} = -vA^m, \tag{7}$$

$$\frac{\mathrm{d}z}{\mathrm{d}t} = -U(x(t),t). \tag{8}$$

The boundary conditions are

$$x=x^*, z=z^* \text{ at } t=0, \tag{9}$$

and

$$x=0, z=0 \text{ at } t=\tau_G. \tag{10}$$

The first boundary condition refers to the present-day landscape, where elevation is z^* at an upstream distance of x^* along a river profile. The landscape response time, τ_G, represents the time taken for a knickzone to propagate from the mouth of a river to any given point, x, upstream. The second boundary condition represents a time in the past, τ_G, where the characteristic curve intersects the river mouth (i.e., $x = 0$ and $z = 0$). Equations (7), (8), and (10) must satisfy

$$\tau_G=\int_0^{x^*}\frac{\mathrm{d}x}{vA^m}. \tag{11}$$

Solutions to equations (7)–(10) take the form

$$\tau_G-t=\int_0^{x(t)}\frac{\mathrm{d}x}{vA^m}, \tag{12}$$

$$z^*=\int_0^{\tau_G}U(x(t),t)\mathrm{d}t. \tag{13}$$

These equations determine the evolution of a single river profile. We have used the algorithm developed by *Rudge et al*. [2015] to simultaneously invert hundreds of river profiles (i.e., multiple observations of x^* against z^*) in order to determine the spatial and temporal evolution of regional uplift. This linear problem can be spatially and temporally discretized by employing a triangular mesh and by specifying a finite number of time steps, respectively. The resultant set of spatial and temporal nodes is represented by a vector, **U**, where intermediate values are obtained by linear interpolation. Since A and x^* are known, equation (8) can be integrated using the trapezoidal rule to yield τ_G. Characteristic curves are calculated from equation (12) and combined with linear interpolation to discretize equation (13) using the trapezoidal rule. In this way, we construct a matrix equation

$$\mathbf{z}=\mathrm{M}\mathbf{U} \tag{14}$$

that describes elevation, **z**, at different loci along observed river profiles. This equation can be inverted to determine **U**. We impose a non-negativity constraint to suppress positive and negative oscillations. Since M usually has fewer rows than columns, it is appropriate to employ a damped least-squares approach. The non-negative least squares (NNLS) inverse problem is solved by minimizing

$$|\mathrm{M}\mathbf{U}-\mathbf{z}|^2+\lambda_S^2|\mathrm{S}\mathbf{U}|^2+\lambda_T^2|\mathrm{T}\mathbf{U}|^2. \tag{15}$$

The essential regularization is imposed using spatial and temporal smoothing parameters, λ_S and λ_T, and their corresponding matrices, S and T, such that

$$|\mathrm{S}\mathbf{U}|^2=\int_S\int_{t=0}^{t_{\max}}|\nabla U|^2\mathrm{d}t\ \mathrm{d}S, \tag{16}$$

and

$$|\mathrm{T}\mathbf{U}|^2=\int_S\int_{t=0}^{t_{\max}}\left|\frac{\partial U}{\partial t}\right|^2\mathrm{d}t\ \mathrm{d}S. \tag{17}$$

We employ a limited-memory Broyden-Fletcher-Goldfarb-Shanno algorithm (L-BFGS-B) to solve this NNLS inverse problem since it is computationally fast and well-suited to sparse matrix problems [*Broyden et al*., 1973].

For significant reasons, we chose not to exploit approaches described by *Goren et al*. [2014] and by *Fox et al*. [2014] who developed alternative linear least squares algorithms that use an empirical Bayesian scheme. In their algorithms, an a priori model of uplift history is selected. This a priori model is based upon a guess of the average uplift rate that is calculated from channel elevation and upstream drainage area. By

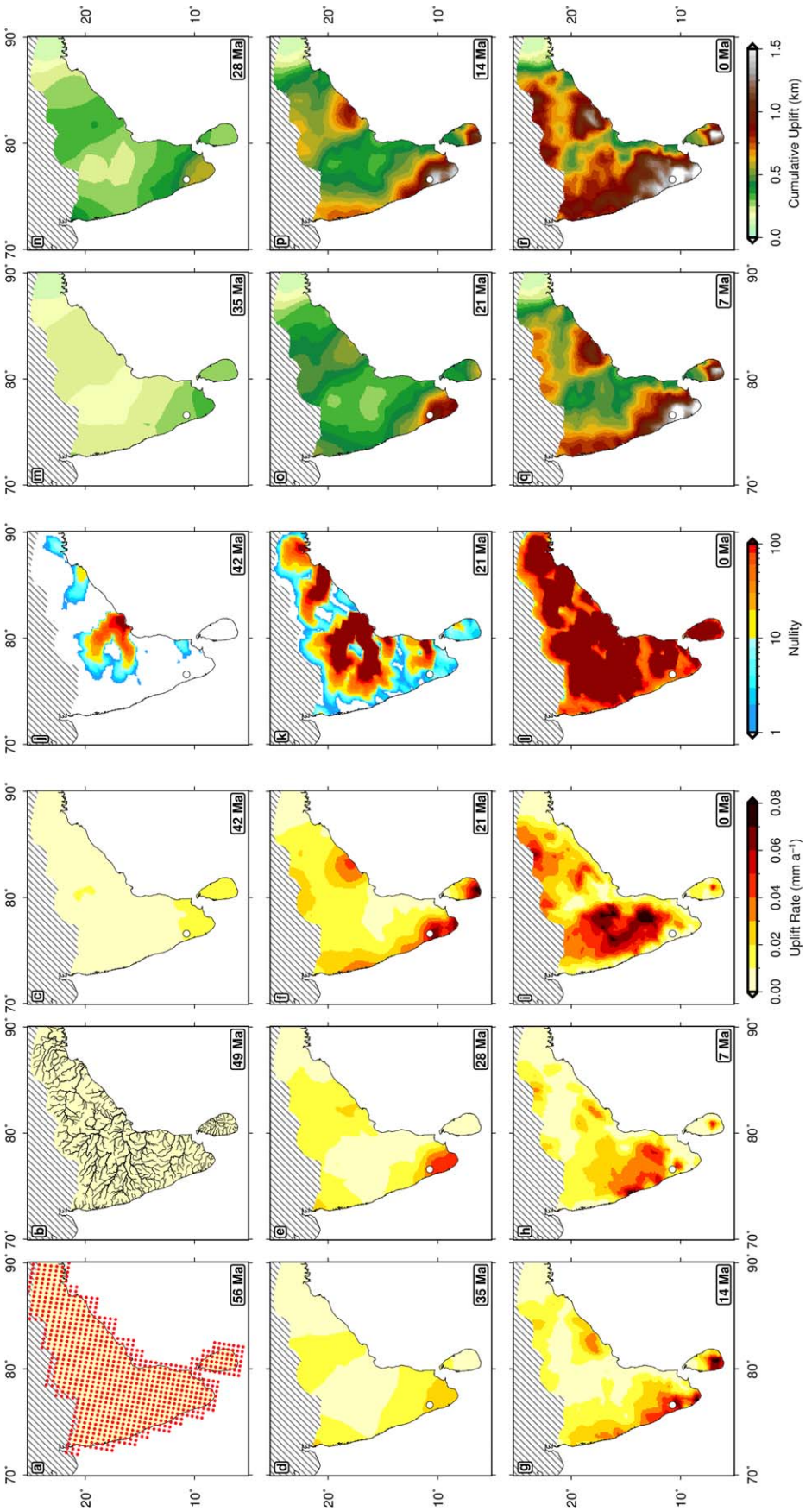

Figure 11. Uplift history of peninsular India. (a) Map showing minimal uplift rate at 56 Ma. Red grid = spatial distribution of nodes at which rock uplift rate, U, is permitted to vary during inverse modeling where $v = 3.7\ m^{0.26}\ Ma^{-1}$, $m = 0.37$, $\lambda_S = \lambda_T = 1$. Hashed polygon = region excluded from inverse modeling. (b) Map showing distribution of drainage network overlain on uplift rate at 49 Ma. (c)–(i) Spatial uplift rate calculated as function of time between 42 and 0 Ma. White circle = location of Palghat Gap (Figure 14). (j)–(l) Nullity plots at 42, 21, and 0 Ma showing number of non-zero entries in model matrix. (m)–(r) Cumulative uplift calculated as function of time between 35 and 0 Ma.

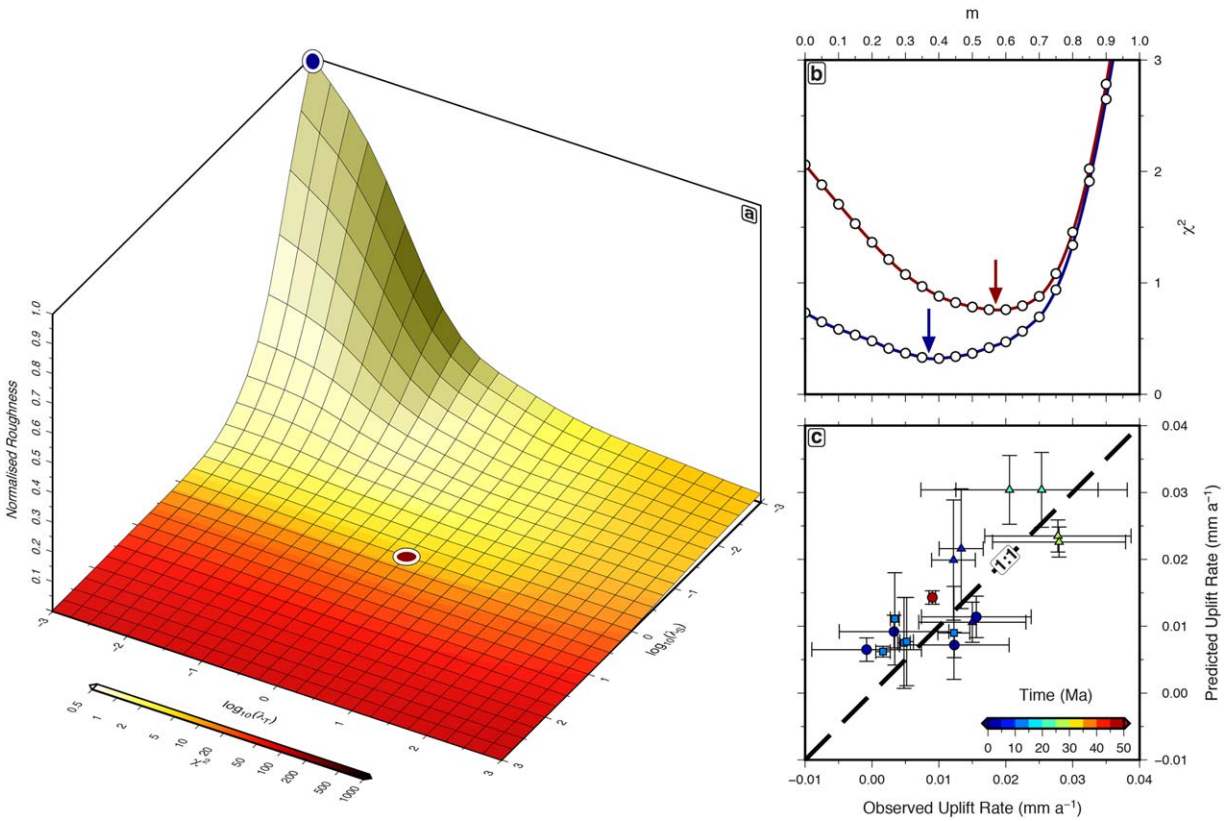

Figure 12. Calibration of model parameters. (a) Model misfit and roughness plotted as function of λ_T and λ_S. Blue/red circles = loci of inverse models where $\lambda_T = \lambda_S = 10^{-3}$ and $\lambda_T = \lambda_S = 1$, respectively. (b) Residual misfit, χ^2, plotted as function of m for $\lambda_T = \lambda_S = 10^{-3}$ (blue curve) and $\lambda_T = \lambda_S = 1$ (red curve). Open circles = calculated values; arrows = loci of global minima at $m = 0.37$ (blue) and at $m = 0.57$ (red). (c) Observed uplift rates from emergent marine terraces (circles), lignite deposits (squares), and incised paleosurfaces (triangles) plotted against calculated rock uplift rates (Table 1). Optimal calculated rates determined by inverse modeling where $v = 3.7^{+0.8}_{-1.2}$ m$^{0.26}$ Ma^{-1}, $m = 0.37$ and $\lambda_T = \lambda_S = 1$. Colored circles/squares/triangles with vertical/horizontal bars = observed versus calculated uplift rates and their uncertainties averaged over different time spans according to scale bar; dashed line = 1:1 relationship. Uncertainty on calculated rates corresponds to upper/lower bounds for values of v whose RMS uplift rate misfit is <125% of global minimum (i.e., $v = 2.5$–4.5 m$^{0.26}$ Ma^{-1}); uncertainty on observed rates corresponds to errors in age and elevation of a given deposit.

updating this a priori model with the observations, an a posteriori model is calculated. This a posteriori model is prevented from straying away from the a priori model and therefore inherits its attributes. In this sense, observational constraints are being exploited twice. *Goren et al.* [2014] do not incorporate spatial and temporal damping. Instead, they chose to damp departures from their a priori model. An important consequence of this approach is that oscillatory behavior can only be reduced by forcing the a posteriori model to stay close to the a priori model. *Fox et al.* [2014] damp spatial gradients of uplift rate by specifying an arbitrary correlation length scale parameter but chose not to damp temporal gradients of uplift rate. Both algorithms achieve best-fit solutions with residual misfits of up to ±150 and ±500 m, respectively.

3.3. Cumulative Uplift History

An inventory of 530 river profiles were simultaneously inverted to determine regional rock uplift rate as a function of space and time (Figures 10 and 11). Residual misfits between observed and calculated river profiles from the major catchments are $\chi^2 \sim 0.5$–1.5. Quality of fit suggests that knickzones are generated when spatially coherent signals propagate through drainage networks according to the stream power formulation. Calculated profiles match laterally continuous, but time-transgressive, paleosurfaces that delineate upland plateaux. These paleosurfaces age upward and tilt eastward with increasing dip [*Gunnell*, 1997; *Bonnet et al.*, 2016]. They attest to a prolonged phase of regional rock uplift that is focussed along the Western Ghats. Vertical separation between paleosurfaces increases through time, which suggests that regional uplift has increased toward the present if these surfaces are equally separated in time.

Calculated cumulative rock uplift histories depend upon the degree of spatial and temporal smoothing and upon the chosen values of the erosional parameters (Figure 11). Here, we have selected $v = 3.7$ and

$m = 0.37$ whose values are determined by independent calibration described below. The values of λ_S and λ_T are chosen to ensure that the smoothest model which yields the smallest misfit between observed and calculated river profiles is obtained for a given set of erosional parameters (i.e., *v*, *m*). To choose the optimal values of λ_S and λ_T, we ran a large suite of individual inverse models for which λ_S and λ_T were simultaneously covaried (Figure 12a). Residual misfit, χ^2, is plotted as a function of λ_S and λ_T so that the smoothest model that yields the best fit between observed and calculated river profiles can be identified [*Parker*, 1994].

We emphasise that identification of the optimal model is neither a precise nor an objective art. Although some misfit reduction inevitably results from the choice of smoothing parameters, visual inspection suggests that NNLS linearized inversion yields small residual misfits along the majority of river profiles. Quality of fit may reflect the lower degree of numerical smearing that is achievable using the method of characteristic curves since it permits finer discretization than non-linear finite difference or finite volume methods with equivalent computation times [*Goren et al*., 2014; *Campforts and Govers*, 2015] (Figure 10). We note that observed and calculated river profiles from the Cauvery catchment have higher residual misfit compared with other major catchments (Figure 10e). It has been suggested that significant residual misfit may be a consequence of river capture events or drainage divide migration that could potentially generate knickzones which would be spatially and temporally inconsistent with respect to a stream-power formulation [*Radakrishna*, 1992; *Fox et al*., 2014].

For the chosen values of *v* and *m*, negligible cumulative rock uplift occurred between 56 and 42 Ma (Figure 11). At 35 Ma, regional uplift commenced at the southern tip of India and propagated northward. By 21 Ma, most of the peninsula appears to have been uniformly uplifted by a total of 300–400 m. The calculated rate of uplift is ≤ 0.02 mm a^{-1} with the exception of the Southern Granulite Terrain and the Deccan Plateau where calculated rates are 0.05–0.06 mm a^{-1} and 0.02–0.03 mm a^{-1}, respectively. The Eastern Ghats experienced an uplift rate of $\sim$0.03 mm a^{-1} but, after 28 Ma, its rate lagged behind that of the Deccan Plateau. Rock uplift of the Southern Granulite Terrain then spread northwestward while uplift of the Deccan Plateau spread southeastward, forming a continuous corridor with a uniform uplift of $\sim$ 500 m along the Western Ghats and Kerala-Konkan coastal plain. Between 21 and 14 Ma, eastward tilt of the Indian peninsula rapidly developed at rates of 0.03–0.08 mm a^{-1} with regional rock uplift focussed along the western margin. During the same period, uplift rates of 0.02–0.04 mm a^{-1} are predicted for the Eastern Ghats. Uplift rate decreased to ≤ 0.06 mm a^{-1} between 14 and 7 Ma but remained focussed on existing elevated areas, apart from a switch to comparatively modest rates at the northern extremity of the western margin. After 7 Ma, the spatial pattern changed again and rock uplift rates of up to 0.07 mm a^{-1} occurred within the central plateaux and along parts of the western margin.

How well resolved is this cumulative uplift history? The spatial distribution of τ_G suggests that Indian river profiles potentially record Cenozoic rock uplift signals (Figure 9). A more rigorous assessment of spatial and temporal resolution is obtained by calculating the number of non-zero values in the model matrix, M, as a function of time (Figures 11j–11l). The spatial distribution of these values shows that uplift signals between $\sim$20 Ma and the present day are well resolved. Prior to $\sim$42 Ma, spatial resolution significantly deteriorates. We conclude that the drainage network is primarily sensitive to Neogene rock uplift signals.

We note that significant Neogene uplift disagrees with the conclusions drawn by *Mandal et al*. [2015a]. Based on the apparent consistency between millennial, ^{10}Be erosion rates and Cenozoic, AFTA rates, they suggested that the landscape of the southern Indian Peninsula is in steady state (i.e., slow isostatic rebound is balanced by landscape erosion). We disagree with their conclusions for two reasons. First, their spatially averaged ^{10}Be erosion rate of 30.8 ± 8.5 m Ma^{-1} is, in fact, significantly greater than the AFTA-derived rates (15–20 m Ma^{-1}). This discrepancy is not consistent with a steady state interpretation [*Gunnell et al*., 2007]. Second, if regional uplift mostly occurred between 35 and 7 Ma, as our inverse modeling suggests, slower millennial erosion rates may simply reflect a subsequent reduction in uplift rate (Figure 11).

3.4. Precipitation

The age of onset of the Indian monsoon is generally considered to be $\sim$8 Ma with two major intensifications after 3.6 Ma [*An et al*., 2001; *Cronin*, 2010]. A significantly earlier onset date of $\sim$15 Ma has also been proposed [*Clift and Plumb*, 2008; *Iaffaldano et al*., 2011]. We have not included variable precipitation in our stream power formulation for three reasons. First, cosmogenic nuclide ^{10}Be studies suggest that no clear link exists between precipitation and erosion rates [*von Blanckenburg*, 2004; *Mandal et al*., 2015a]. Second, it

Table 1. Observed and Calculated Uplift Rates for Peninsular India

Locality	Longitude	Latitude	Age Range (Ma)	Elevation Range (m)	Obs. Uplift Rate (mm a^{-1})	Pred. Uplift Rate (mm a^{-1})	Constraints
Jhimili	79.16	22.05	64.9 ± 0.1 – Present	0^{+30}_{-25} – 591	0.009 ± 0.001	0.014 ± 0.001	[a]
Kappataswamy	76.51	14.96	27.5 ± 0.8 – Present	250 ± 250 – 1019	0.028 ± 0.010	0.022 ± 0.002	[b]
Channanghi	76.58	14.95	26.3 ± 1.3 – Present	250 ± 250 – 981	0.028 ± 0.011	0.023 ± 0.002	[b]
Triveni	75.43	13.84	23.9 ± 0.2 – Present	300 ± 300 – 906	0.025 ± 0.013	0.030 ± 0.006	[b]
Kumsi	75.42	14.05	23.2 ± 0.3 – Present	300 ± 300 – 777	0.021 ± 0.013	0.030 ± 0.005	[b]
Naveli	74.18	15.17	8.7 ± 0.2 – Present	25 ± 25 – 141	0.013 ± 0.003	0.022 ± 0.009	[b]
Caurem	74.08	15.13	8.7 ± 0.2 – Present	25 ± 25 – 131	0.012 ± 0.003	0.020 ± 0.009	[b]
Cudnem	74.08	15.13	2.5 ± 0.2 – Present	12.5 ± 12.5 – 50	0.015 ± 0.008	0.011 ± 0.003	[b]
Neyveli	79.46	11.45	11.2 ± 5.6 – Present	0^{+15}_{-5} – 18	0.002 ± 0.001	0.006 ± 0.001	[c]
Parchuri	73.48	17.14	10.9 ± 2.9 – Present	0^{+15}_{-5} – 169	0.012 ± 0.002	0.009 ± 0.007	[d]
Malvan	73.49	16.10	10.9 ± 2.9 – Present	0^{+15}_{-5} – 42	0.003 ± 0.001	0.001 ± 0.007	[e]
South Ratnagiri	73.32	16.93	10.9 ± 2.9 – Present	0^{+15}_{-5} – 61	0.005 ± 0.001	0.008 ± 0.001	[f]
North Ratnagiri	73.30	17.02	10.9 ± 2.9 – Present	0^{+15}_{-5} – 67	0.005 ± 0.001	0.008 ± 0.001	[f]
Rameswaram	79.33	9.31	0.122 ± 0.005 – Present	3.0 – 2.9 ± 1	−0.001 ± 0.008	0.006 ± 0.002	[g]
Idindakarai	77.75	8.18	0.122 ± 0.005 – Present	3.0 – 3.4 ± 1	0.003 ± 0.008	0.009 ± 0.002	[g]
Manappad	78.07	8.37	0.122 ± 0.005 – Present	3.0 – 4.5 ± 1	0.012 ± 0.008	0.007 ± 0.002	[g]
Cape Comorin	77.50	8.09	0.122 ± 0.005 – Present	3.0 – 4.9 ± 1	0.016 ± 0.008	0.011 ± 0.003	[g]

[a] *Keller et al*. [2009]: magnetostratigraphic dating of shallow marine intertrappean beds.
[b] *Bonnet et al*. [2016]: $^{40}Ar/^{39}Ar$ dating of cryptomelane from weathering profiles beneath lateritic paleosurfaces.
[c] *Singh et al*. [1992], [d] *Brückner* [1987], [e] *Kumaran et al*. [2004], [f] *Suryawanshi and Golekar* [2014]: biostratigraphic dating of lignite deposits.
[g] *Banerjee* [2000]: U/Th dating of emergent marine terraces.

has been argued that no appreciable change in spatially averaged precipitation rates occurred over the Indian peninsula since Eocene times [*Reuter et al*., 2013; *Shukla et al*., 2014]. Finally, it has been shown that varying precipitation rate only affects calculated rock uplift histories if it has a periodicity of several million years or more [*Paul et al*., 2014; *Wilson et al*., 2014; *Stephenson et al*., 2014].

Nevertheless, there is likely to be positive feedback between precipitation pattern and topographic relief [*Gunnell*, 1997]. Modern precipitation patterns can be orographically controlled and the monsoon intensification observed between 15 and 8 Ma could be related to the Western Ghats having reached some threshold elevation [*Nair*, 2006]. Faunal and floral shifts in Early to Mid-Miocene (23–14 Ma) times suggest that a topographic barrier did develop, implying that Neogene growth of the Western Ghats and modification of precipitation patterns are indeed coupled [*Van Bocxlaer et al*., 2009; *Kern et al*., 2013].

4. Calibration and Testing

4.1. Erosional Parameters

The calculated cumulative rock uplift history presented in Figure 11 is predicated upon having selected particular values of v and m. We have used an objective strategy to choose v and m by exploiting the computational speed of the NNLS linear inverse algorithm. First, it is straightforward to carry out a parameter sweep where m is varied at increments of 0.05 between 0 and 1 with minimal damping (i.e., $\lambda_S = \lambda_T = 10^{-3}$; Figure 12b). This systematic sweep reveals that there is a weak global minimum at $m = 0.37^{+0.16}_{-0.11}$ where the quoted uncertainty reflects values of m that yield misfit values $> 125\%$ of that at the global minimum. This range of values broadly agrees with published estimates [*Stock and Montgomery*, 1999; *van der Beek and Bishop*, 2003; *Mandal et al*., 2016]. The shape of the misfit function emphasises that m is unlikely to have a fractional value significantly greater than 0.5.

λ_S and λ_T are then co-varied between 10^{-3} and 10^{3} for $m = 0.37$ to identify the smoothest model that yields the smallest residual misfit (Figure 12a). The chosen optimal model is at $\lambda_S = \lambda_T = 1$. If the parameter sweep for m is repeated for these values of λ_S and λ_T, the global minimum shifts to $m = 0.57^{+0.15}_{-0.21}$ (Figure 12b). We acknowledge that a weak positive trade-off exists between m and the values of λ_S and λ_T. This trade-off is expected: a highly damped inverse model can only find an appropriately small misfit between observed and calculated river profiles by increasing the rate of incision which is achievable by increasing m. To address this issue, we note that the suite of observed and calculated rock uplift rates should also agree, subject to the negative trade-off that exists between m and v [*Roberts and White*, 2010]. When $m = 0.37$, there is an improved fit ($\sim 20\%$) between calculated and observed uplift rates than when $m = 0.57$, irrespective of

the value of v applied at either value of m (Figure 12c). We note that $m = 0.37$ falls within a statistically acceptable range of misfit tolerance for $\lambda_S = \lambda_T = 1$. We therefore apply a value of $m = 0.37$ as this fits uplift rate constraints better than higher values, whilst simultaneously yielding acceptable fits between observed and modeled river profiles.

The value of v sets the pace for landscape erosion but it does not directly affect the residual misfit between observed and calculated rivers. Since published values of v have considerable variation, we have chosen to determine its value solely by calibration against independent rock uplift rate estimates (Figure 12c and Table 1). These estimates comprise U/Th dates from emergent marine terraces, heights, and biostratigraphic ages of lignite deposits, together with elevations and magnetostratigraphic ages of shallow marine intertrappean horizons. We also consider $^{40}Ar/^{39}Ar$ dates from lateritized paleosurfaces whose original elevation is uncertain.

Although measurements are sparse, U/Th dates from Marine Isotopic Stage (MIS) 5e coral terraces that are exposed at 3–15 m above sea level along the west coast. These dates imply a NW-SE gradient of rock uplift rate from 0.1 to 0.02 mm a^{-1} (this range is 0.09 to 0.0 mm a^{-1} when corrected for MIS 5e sea level of 3 m) [*Siddall et al*., 2006; *Pedoja et al*., 2011]. The highest terraces crop out along the Saurashtra coast where rift structures have been reactivated as reverse faults [*Bodin and Horton*, 2004]. Elevated terraces also occur in tectonically inactive regions such as Kerala (Figure 1c). Holocene emergent marine terraces and raised beach deposits that were dated using ^{14}C and U/Th techniques are also exposed 2–3 m above sea level along the west coast. These features are typically ~1 m higher than equivalent features exposed along the east coast, suggesting that long-wavelength tilting is ongoing [*Banerjee*, 2000; *Alappat et al*., 2015] (Figure 7b). The youthfulness of these terraces and deposits, combined with the possible existence of a mid-Holocene eustatic highstand, implies that reliable long-term uplift rates cannot be extrapolated [*Woodroffe and Horton*, 2005; *Kench et al*., 2009].

Extensive lignite horizons, dominated by mangrove swamp flora, are found within the Mio-Pliocene Warkalli and Cuddalore Formations on both sides of the peninsula. Along the west coast at Malvan, lignites are exposed at elevations of 80–150 m. On the east coast at Neyveli, similar deposits occur at 10 m (Figure 7b). Additional evidence for Neogene uplift along the west coast comprises shallow marine deposits of the Late Burdigalian to Early Langhian (~15 Ma) Quilon Formation. These deposits are now exposed at elevations of up to 92 m in the hinterland of the Kerala coastal plain (Figure 7b) [*Singh*, 1998; *Reuter et al*., 2013].

The existence of ~65 Ma old intertrappean shallow marine deposits at elevations of ~600 m near Jhimili indicates that regional topography was subdued following the main phase of Deccan volcanism. Present-day topography is inferred to have grown significantly in the intervening period [*Keller et al*., 2009]. This inference in conjunction with the subsequent onset of pervasive lateritization suggests that regional relief was probably modest during Eocene and Oligocene times. Studies that combine digital elevation models with $^{40}Ar/^{39}Ar$ dating of cryptomelane suggest there are up to three topographically concordant lateritic paleosurfaces in the western highlands [*Gunnell*, 1998; *Bonnet et al*., 2014, 2016]. These deposits crop out at elevations of 650–1200 m and have ages of 23–53 Ma. If these lateritic paleosurfaces originally formed at elevations of 0–600 m, we infer rock uplift rates of 0.02–0.03 mm a^{-1} since 23 Ma [*Widdowson*, 1997; *Sheth*, 2007; *Bonnet et al*., 2014]. The inferred range of 0–600 m is conservative and the higher value is determined from the average elevation above sea level of valleys that incise these paleosurfaces. We have also included uplift rates estimated from the separation of stacked paleosurfaces and from the youngest $^{40}Ar/^{39}Ar$ ages obtained from underlying weathering profiles. These values assume that the youngest ages represent abandonment of the paleosurface and onset of incision [*Beauvais and Chardon*, 2013].

A parameter sweep, where v was varied at increments of 0.1 between 2.2 and 5.2 $m^{0.26}$ Ma^{-1}, was used to identify the value of v which minimizes the misfit between observed and calculated rock uplift rates. For $m = 0.37$, the optimal value of v is $3.7^{+0.8}_{-1.2}$ $m^{0.26}$ Ma^{-1}. The upper and lower bounds correspond to values of v that yield root mean square (RMS) misfit values $< 125\%$ of its value at the global minimum.

4.2. Independent Tests

Spot measurements of observed and calculated rock uplift rates are in reasonable agreement. Nevertheless, it is important to ensure that the cumulative rock uplift history presented in Figure 11 is tested against a geographically and temporally broader set of onshore and offshore observations. Here, we consider the

growth and distribution of lateritized surfaces, low-temperature thermochronologic measurements, solid sedimentary flux measurements at major deltas and offshore sequence stratigraphic architecture [*Halkett*, 2002; *Gunnell et al*., 2003; *Sahu et al*., 2013; *Mandal et al*., 2015b]. It is important to emphasize that these tests are independent of the calibration of the erosional parameter *v* that was used to calculate the cumulative uplift history.

4.2.1. Lateritized Paleosurfaces

Extensive laterite deposits are consistent with a prolonged period during which relief was subdued and regional climate was sufficiently humid for thick ($\leq$ 200 m) chemical weathering deposits to develop (Figure 7a). These lateritized surfaces are often deeply incised, which suggests that their present-day elevation is disequilibrated with respect to the modern landscape. An important corollary is that they probably formed at lower elevations [*Widdowson*, 1997]. Although these surfaces are heavily dissected, they exhibit low relief and are topographically continuous, suggesting that they represent former base levels that once graded toward sea level [*Valeton*, 1983; *Chardon et al*., 2006]. Development of Western Ghats laterites that drape Deccan basalts demonstrates that they are post-Cretaceous in age [*Widdowson and Cox*, 1996]. Studies that combine high-resolution digital elevation models with $^{40}Ar/^{39}Ar$ dating of cryptomelane suggest there are up to three topographically concordant lateritic paleosurfaces in the western highlands whose ages range between 52 and 23 Ma [*Gunnell*, 1998; *Bonnet et al*., 2014, 2016]. These time-transgressive surfaces, with the oldest, increasingly tilted ones cropping out at the greater elevation, point toward successive cycles of incision, and valley widening in response to changes in base level followed by topographic quiescence [*Green et al*., 2013]. If these stacked surfaces represent former base levels that developed at similar elevations, rock uplift rates of $<$ 0.02 mm a^{-1} can be inferred. After 23 Ma, laterite formation within the uplands appears to have ceased. The current elevation of these surfaces (1200–650 m) together with their strongly incised appearance point toward a rapid increase in relief during Neogene times. Any such increase during this period would limit lateral channel migration and the extensive planation required to form these surfaces [*Widdowson*, 1997; *Sheth*, 2007; *Bonnet et al*., 2014].

The situation for lower-lying areas is less clear since there is considerable debate about the interpretation of $^{40}Ar/^{39}Ar$ weathering dates and their relationship to paleosurface evolution. Paleomagnetic ages suggest that the lowland surface developed in Late Cenozoic times whereas those from elevated uplands yield Early Cenozoic ages [*Schmidt et al*., 1983]. However, in the western lowlands near Goa, two ages of $\sim$46 Ma have been obtained for a weathered profile beneath a lateritized lowland plateau at $\sim$150 m elevation [*Beauvais et al*., 2016]. This pediment is capped by ferricrete composed of reworked and cemented lateritic clasts [*Bonnet et al*., 2016]. It has been suggested that some lowland laterites are allochthonous, having been generated by the dissection and gravitational collapse of upland surfaces [*Fox*, 1923; *Ghosh and Guchhait*, 2015]. However, if the dated material did precipitate in situ, preservation of these ages on either side of the escarpment suggests either that there was differential rock uplift between the uplands and lowlands between $\sim$23 and 9 Ma or that the Western Ghats escarpment has been close to its present-day position with similar relief since $\sim$60 Ma.

This latter possibility, invoked by *Beauvais et al*. [2016], necessitates escarpment formation by $\sim$60 Ma with minimal subsequent denudation. It cannot easily be reconciled with 1–1.5 km of denudation following eruption of Deccan basalts that is required to form the Konkan coastal plain. It also disagrees with thermochronologic evidence for significant post-40 Ma denudation at rates of $\sim$60 m Ma^{-1} across the Kerala-Konkan lowlands since Late Miocene times [*Kalaswad et al*., 1993; *Gunnell et al*., 2003; *Campanile et al*., 2008; *Mandal et al*., 2015a]. These rates are consistent with cosmogenic nuclide studies and with evidence for ongoing escarpment retreat [*Mandal et al*., 2015b, 2016]. Differential uplift could have occurred as a result of a combination of offshore sedimentary loading and onshore denudational unloading that is manifest in seaward downwarping of the lowland pediment. Nevertheless, these surfaces are evidently not cogenetic since one forms on the original crest of the Deccan lava pile and the other is demonstrably located by as much as 1–1.5 km within the interior of the same lava pile [*Widdowson and Cox*, 1996; *Campanile et al*., 2008]. We maintain that the most plausible explanation is that a progressive drop in regional base level triggered by Neogene uplift caused the development and preservation of lateritic paleosurfaces with the lowland surface postdating its time-transgressive upland counterparts. We acknowledge that it is difficult to reconcile the earliest Cenozoic $^{40}Ar/^{39}Ar$ dates from the lowland pediment with abundant and convincing evidence for post-Neogene uplift and denudation (e.g., emergent marine and lignite deposits, incision of paleosurfaces, thermochronologic observations, and sedimentary flux measurements).

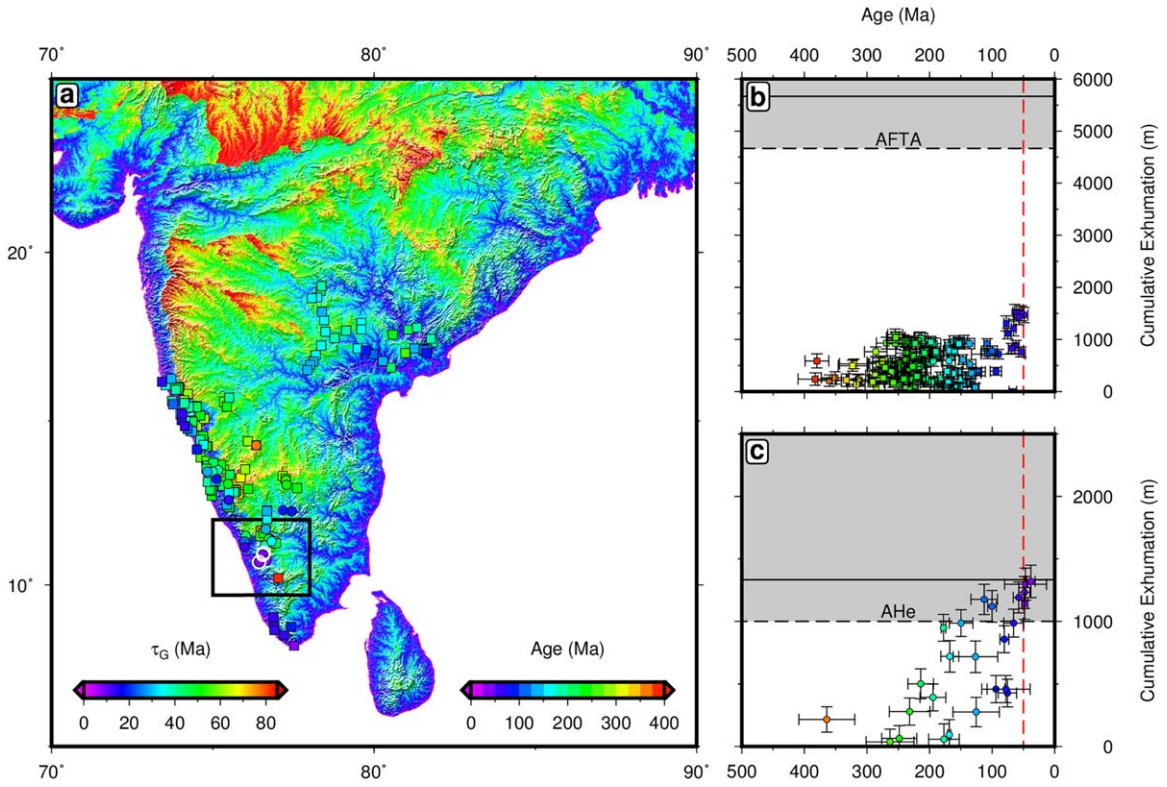

Figure 13. Comparison of thermochronologic measurements and calculated exhumation. (a) Map of landscape response time, τ_G, calculated from drainage catchments. Colored squares/circles = AFTA/AHe ages [*Gunnell et al.*, 2003; *Sahu et al.*, 2013; *Mandal et al.*, 2015b]; black box = location of Palghat Gap (Figure 14a); white circles = locations of AHe samples whose cooling histories are shown in Figures 14c–14e. (b) Calculated exhumation plotted as function of AFTA age. Solid line = mean exhumation since 50 Ma required to record $\leq$ 50 Ma AFTA age; gray band with dashed lines = envelope reflecting uncertainties in mean surface (25 $\pm$ 5 °C) and closure temperatures (110 $\pm$ 10 °C), assuming constant geothermal gradient of 15 °C km^{-1} [*Roy and Rao*, 2000; *Agrawal and Pandey*, 2004]. Exhumation since 50 Ma calculated using $v = 3.7^{+0.8}_{-1.2}$ m$^{0.26}$ Ma^{-1} and $m = 0.37$ for $\lambda_S = \lambda_T = 1$. (c) Calculated exhumation plotted as function of AHe ages. Solid line = mean exhumation since 50 Ma required to record $\leq$ 50 Ma AHe age; gray band with dashed lines = envelope reflecting uncertainties in mean surface and closure temperatures (57.5 $\pm$ 12.5 °C), assuming constant geothermal gradient. Uncertainty on predicted cumulative exhumation corresponds to values for upper/lower bounds on *v*; uncertainty on sample ages corresponds to 1σ error.

Warm and humid climatic conditions are probably key prerequisites for the formation of laterites [*Widdowson and Mitchell*, 1999]. Present-day rainfall patterns preclude laterite formation in parts of the high plateaux to the east of the Western Ghats escarpment. These patterns are primarily controlled by the orographic effect associated with the Western Ghats [*Fawcett*, 1994; *Tawde and Singh*, 2015]. Palynologic evidence suggests that temperature and precipitation were both sufficiently high to permit laterites to form across lowland areas throughout Cenozoic times [*Meher-Homji*, 1989; *Brückner*, 1992]. The existence of an orographic effect would suggest that time-transgressive lateritization of southern Indian paleosurfaces between 53 and 23 Ma could be accounted for by a steady increase in elevation. This interpretation could explain the abrupt cessation of upland laterite formation because uplift of the Western Ghats beyond a threshold elevation would trigger an orographic climatic regime with precipitation increasingly concentrated along the coastline and reduced in the interior.

An alternative hypothesis is that these plateaux were already elevated and that dating of cryptomelane records a rapid post-23 Ma lowering of the elevation window within which humidity and temperature were appropriate for laterite formation [*Beauvais et al.*, 2016; *Bonnet et al.*, 2016]. This hypothesis requires the existence of both significant relief and widespread high precipitation rates (e.g., $>$1 m a^{-1}) between 52 and 23 Ma [*Thorne et al.*, 2012]. Such conditions are at odds with the notable absence of clastic sedimentary flux into the principal deltas during this period (Figure 7a). The orographic interpretation of laterite ages is more consistent with these observations and permits the inclusion of paleosurficial elevations for calibration purposes. Significantly, if these ^{40}Ar/^{39}Ar dates are omitted, the calibrated value of *v* is unchanged, although its uncertainty increases.

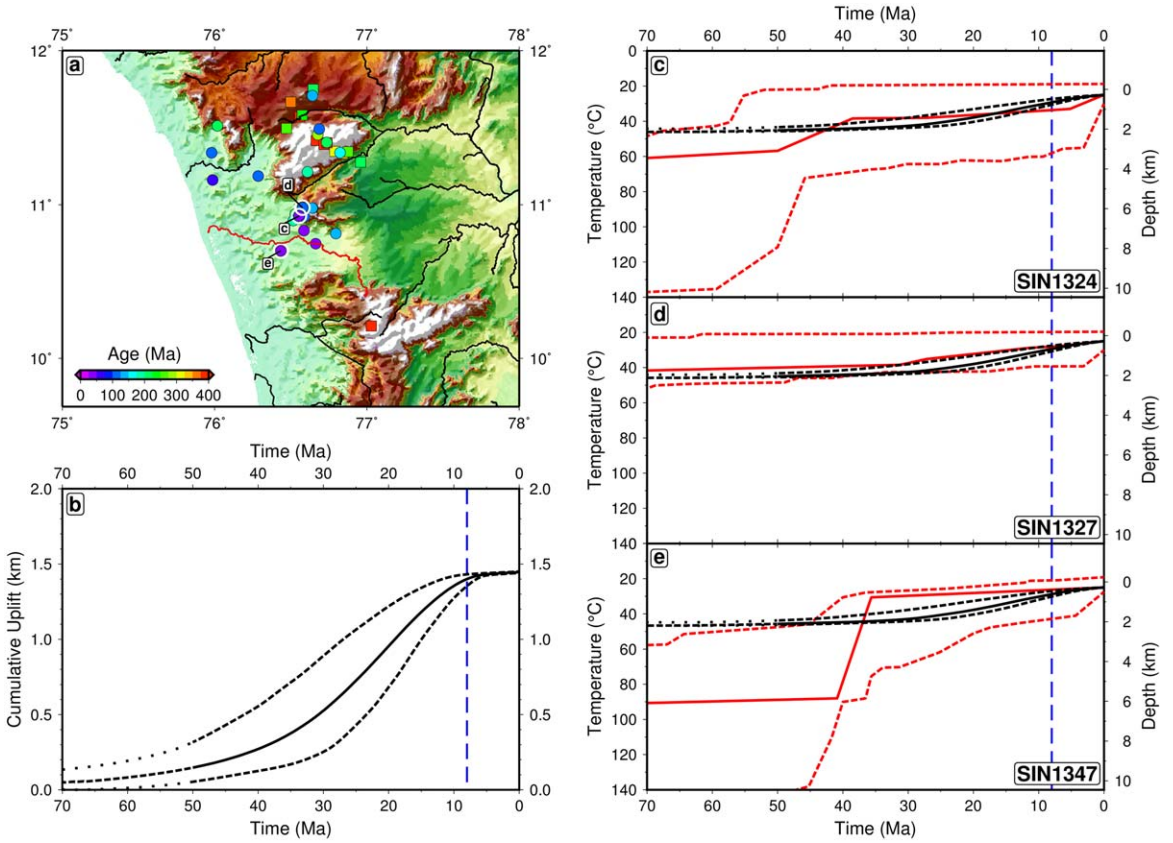

Figure 14. Thermochronologic measurements and denudation history at Palghat Gap. (a) Map of Palghat Gap region. Colored circles/squares = AFTA/AHe dates [*Gunnell et al.*, 2003; *Mandal et al.*, 2015b]. Black lines = drainage, red line = location of Bharathappuzha river whose incision history is shown in Figures 14c–14e; white circles = locations of samples SIN1324, SIN1327, and SIN1347 from *Mandal et al.* [2015b] used to construct time-temperature relationships in Figures 14c–14e. (b) Calculated cumulative uplift history of Palghat Gap region for $v = 3.7^{+0.8}_{-1.2}$ $m^{0.26}$ Ma^{-1} and $m = 0.37$. Solid/dashed lines = mean cumulative uplift history with uncertainty corresponding to values for upper/lower bounds on v; dotted lines = poorly constrained history for period when $\geq$ 50% of model nodes are null; dashed blue line = onset of monsoon intensification at 8 Ma. (c) Denudation history of Palghat Gap region for sample SIN1324. Solid/dashed lines = mean incision history at closest point along river to SIN1324 with uncertainty corresponding to values for upper/lower bounds on v; dotted lines = poorly constrained incision history as before; red solid/dashed lines = statistically favored time-temperature (*T-t*) paths for SIN1324 with envelope of "acceptable" *T-t* paths ($p > 0.05$) generated by HeFTY algorithm [*Ketcham*, 2005]. Depth axis calculated by assuming geothermal gradient of 15 °C km^{-1} [*Roy and Rao*, 2000; *Agrawal and Pandey*, 2004]. (d) Denudational history for sample SIN1327. (e) Denudational history for sample SIN1347.

4.2.2. Thermochronology and Denudation

Apatite fission track ages are consistently older than 55 Ma with short track lengths. This distribution suggests a complex denudation history that cannot be attributed to a single cooling event [*Gunnell et al.*, 2003]. Similar denudation histories are recovered across eastern India with a late Cenozoic peak observed in the *T-t* (temperature-time) relationships derived from many samples [*Sahu et al.*, 2013]. The inferred low geothermal gradient for India (i.e., 15 °C km^{-1}) suggests that, for a stable geothermal profile, exhumation of 4.7–6.7 km is required to cool samples now found at the surface through their closure temperatures (i.e., 110 ± 10 °C, depending on cooling rate) [*Dodson*, 1973; *Roy and Rao*, 2000; *Agrawal and Pandey*, 2004; *Lisker et al.*, 2009]. The paucity of Cenozoic ages suggests that no more than 4.7 km of exhumation has occurred since 65 Ma. However, this conclusion yields little insight into potentially significant Cenozoic denudation below this threshold. The apatite (U-Th-Sm)/He (AHe) system has a closure temperature of 45–70 °C, depending upon cooling rate, and is therefore capable of resolving exhumation within the 1–3.3 km range [*Zeitler et al.*, 1987; *Wolf et al.*, 1996; *Farley*, 2000]. Although only one AHe study has been published, it yields Mesozoic ages for samples from elevated sections of the Western Ghats Escarpment with ages ~40 Ma from the Palghat Gap [*Mandal et al.*, 2015b]. This distribution suggests negligible erosion (> 1 km) throughout Cenozoic times on relict paleosurfaces and inselbergs within the highlands, followed by rapid Neogene denudation (> 1 km) in the vicinity of major rivers that drain the Nilgiri and Kodakainal plateaux. The *T-t* relationships from these studies provide strong evidence for Cenozoic rock uplift and denudation with the

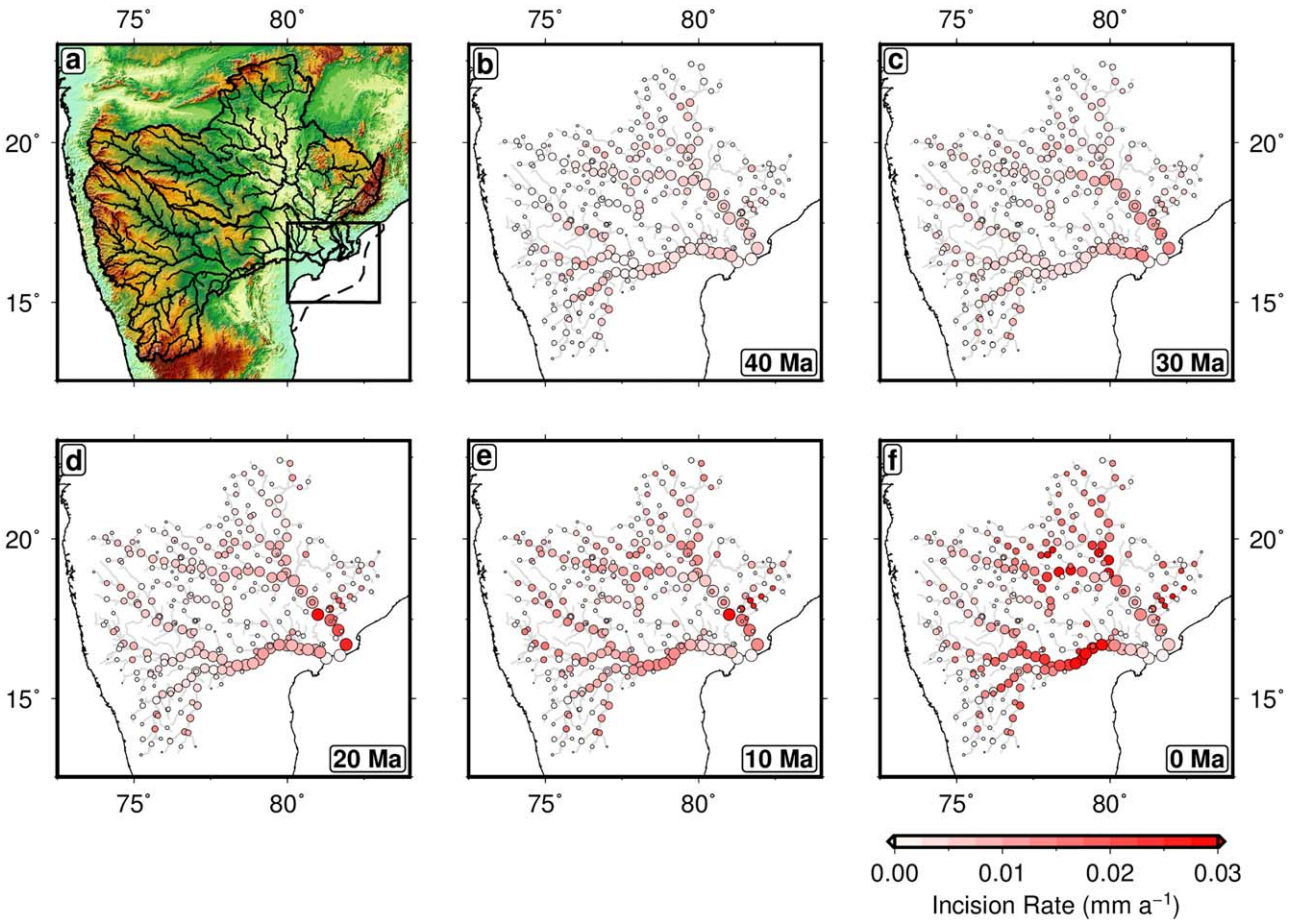

Figure 15. Predicted incision history of Krishna & Godavari catchments. (a) Topographic map of central India. Thick black line = outline of Krishna and Godavari catchments; thin black lines = principal rivers and their tributaries; black box = Krishna-Godavari delta region shown in Figure 16; dashed line = edge of offshore delta; (b) Predicted incision rates calculated at 40 Ma for $v = 3.7\ m^{0.26}\ Ma^{-1}$, $m = 0.37$ and $\lambda_S = \lambda_T = 1$ (see scale bar). Gray lines = drainage within catchment. (c)–(f) Predicted incision rates at 30, 20, 10, and 0 Ma.

greatest erosion confined to major rivers and minimal erosion of low-relief paleosurfaces stranded at high elevation along the principal watersheds.

Denudational histories recovered by inverse modeling of drainage networks can be compared with thermochronologic estimates (Figure 13). By assuming Cenozoic geothermal gradients and average surface temperatures equivalent to those of the present day (~15 °C km^{-1} and 25 ± 5 °C, respectively), we can convert observed *T-t* histories for different AFTA and AHe samples into time-exhumation (*T-z*) histories. These histories can then be compared with calculated denudational values obtained by inverse modeling. Predicted cumulative denudation is calculated by subtracting modern topography from the cumulative rock uplift predicted by the inversion between a given time step and the present day. This approach is predicated on the existence of negligible topography at 50 Ma and so it represents an upper limit for cumulative denudation.

We perform this calculation from 50 Ma onward since this period is one for which inverse modeling yields adequate spatial coverage (Figure 13a). By comparing these predicted values with thermochronologic measurements for India, it is straightforward to demonstrate that Neogene epeirogeny has not generated sufficient exhumation to be recorded by apatite fission track analysis (i.e., 4.7–6.7 km or 100–120 °C cooling; Figure 13b). However, where predicted denudation is large enough to cross the lower AHe closure temperature threshold of 45–70 °C (i.e., 1–3.3 km), ages younger than 50 Ma are obtained (Figure 13c). This observation, combined with an obvious age-cumulative exhumation correlation for both AFTA and AHe samples, shows that Neogene denudation has left a clear and pervasive signal within basement rocks of the coastal plain. This result also agrees with 1–1.5 km Cenozoic denudation estimates for the Kerala-Konkan coastal

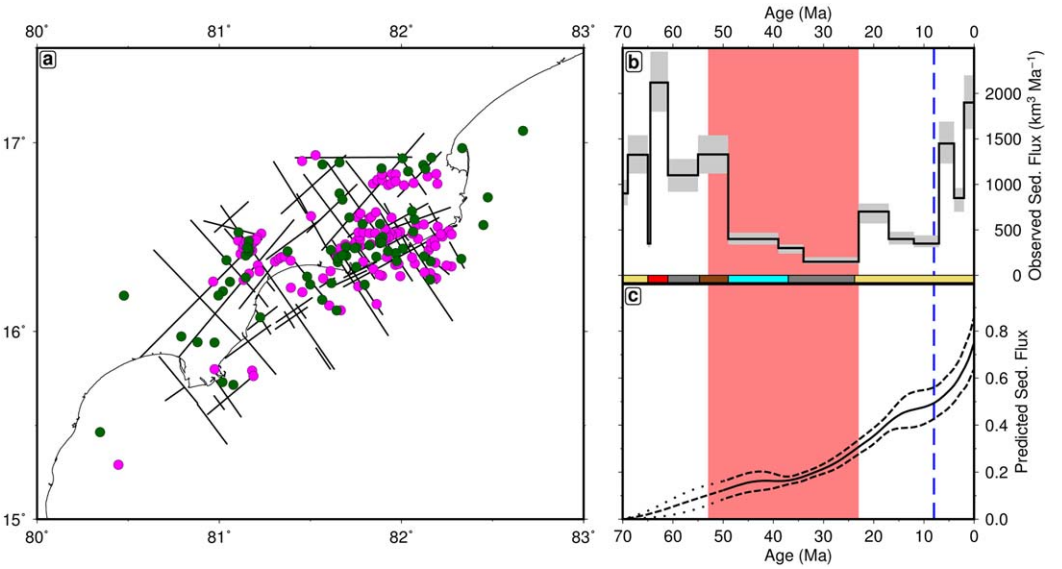

Figure 16. Testing uplift histories against sedimentary flux observations. (a) Map of seismic reflection survey and wells from Krishna-Godavari delta (see Figure 15 for location). Solid lines = seismic profiles; magenta circles = wells without sonic logs; green circles = well with sonic logs. (b) Sedimentary flux history of delta calculated using seismic survey calibrated by well data [*Halkett*, 2002]. Solid line and gray band = mean sedimentary flux $\pm 1\sigma$; horizontal color bar shows lithology (yellow = sandstone, blue = limestone, gray = mudstone, red = volcanic rocks, brown = siltstone); red vertical band = period of laterite formation for Western Ghats [*Bonnet et al*., 2016]; dashed blue line = onset of monsoon intensification at 8 Ma. (c) Predicted sedimentary flux for $v = 3.7^{+0.8}_{-1.2}$ $m^{0.26}$ Ma^{-1}, $m = 0.37$ and $\lambda_S = \lambda_T = 1$. Solid/dashed lines = mean predicted sedimentary flux with uncertainty corresponding to values for upper/lower bounds on v; dotted lines = period when model resolution is less good.

plain calculated from basaltic stratigraphy by *Widdowson and Cox* [1996]. These estimates suggest that the 3–4 km estimated by *Gunnell et al*. [2003] from thermochronologic modeling and the <250 m value estimated by *Beauvais et al*. [2016] from lowland paleosurfaces are upper and lower limits, respectively.

For a given rock uplift rate history, the shape of a river profile can be reconstructed through time. The integrated erosion between reconstructed river profiles at two different time steps constrains the volume of rock removed during that period. We have carried out this calculation for the Bharathappuzha river that drains the Palghat Gap in order to determine an incision rate history which can be compared with the AHe *T-t* histories calculated by *Mandal et al*. [2015b] (Figures 14a and 14b). This comparison reveals clear evidence for post-50 Ma uplift and incision (Figures 14b–14e). This incision history fits the mean *T-t* path for post-50 Ma AHe samples, falling within 95% probability bounds (Figures 14c–14e). Crucially, onset of more rapid cooling after 40 Ma broadly coincides with increased incision. It also immediately postdates the initiation of rapid uplift, although the exact timing of cooling varies between samples (Figures 14b–14e). We also record sufficient incision (i.e., ≥ 1.33 km for a 45 °C closure temperature) to record an AHe age but not an AFTA age.

4.2.3. Solid Sedimentary Flux Estimates

Circumstantial evidence for Neogene uplift is provided by a post-23 Ma switch from carbonate to clastic-dominated sedimentation within offshore deltas (Figures 7a and 7b) [*Raju*, 2008]. This switch to clastic deposition clearly predates onset of monsoon intensification at 8 (or 15) Ma, although the exact timing of intensification is uncertain [*Burckle*, 1989; *Kroon et al*., 1991; *Wang et al*., 2005; *Clift*, 2010]. Cosmogenic nuclide studies suggest that erosion rates are less sensitive to precipitation but that they primarily scale with channel gradient and relief. This suggestion implies that rock uplift, and not climate per se, is primarily responsible for the switch [*Mandal et al*., 2015a].

Here, we investigate the relationship between cumulative rock uplift history and sedimentary efflux in more detail. Our calculated uplift histories can be tested by attempting to match observed sedimentary deposition at major deltas. By carrying out incision calculations for all non-repeating sections of river profiles within the Krishna and Godavari catchments, we determine an incision rate history for the two largest catchments of the Indian Peninsula (Figure 15). By integrating these incision rates over time, we

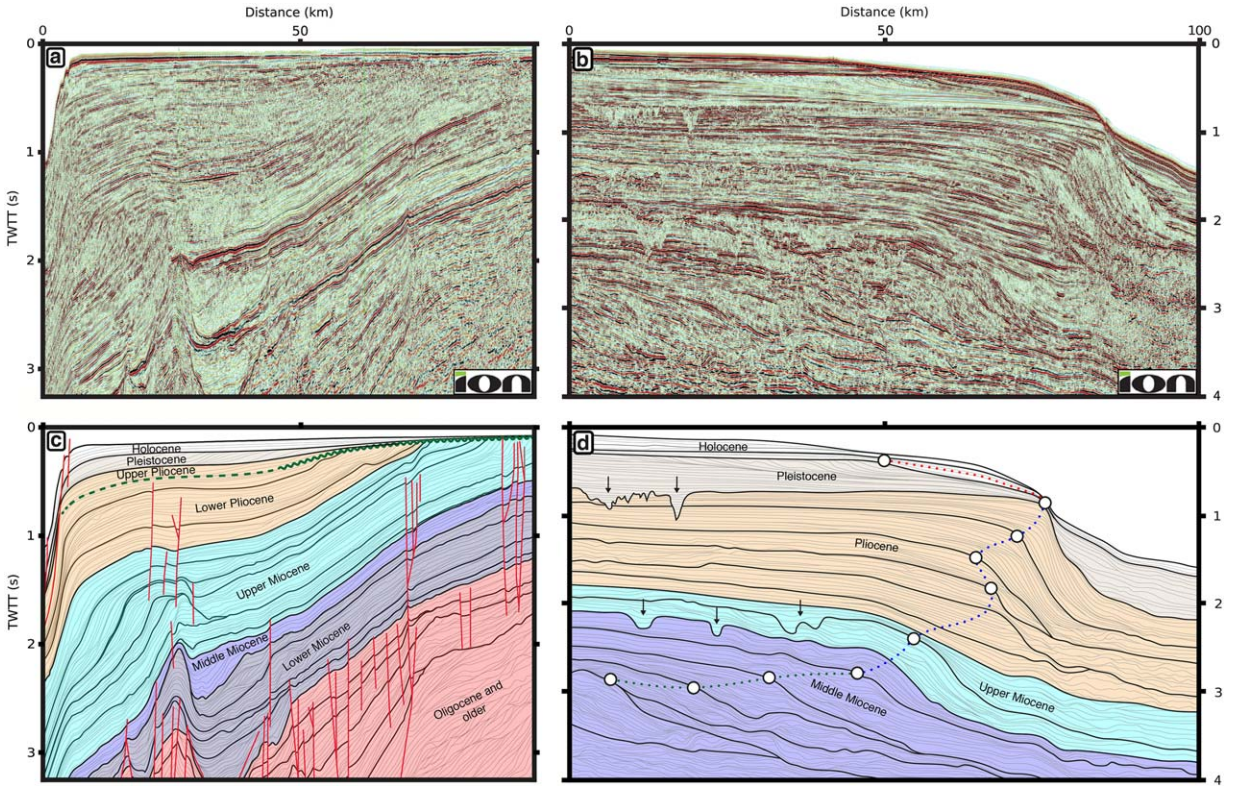

Figure 17. Seismic profiles from Indian margins. (a) Profile located offshore Saurashtra on western shelf. (b) Profile from edge of Mahanadi Delta on eastern shelf. (c) Interpretation of Figure 17a. Wiggly/dashed green line = angular unconformity with transition into sequence boundary; thin/gray lines = depositional/other boundaries; red lines = normal faults. Note top sets truncated by post-16 Ma angular unconformity. (d) Interpretation of Figure 17b. White circles = clinoformal crests; green/blue/red circles = progradational/aggradational/retrogradational depositional sequences within Mio-Pliocene strata representing ~600 m of water-loaded subsidence; black arrows = paleochannels.

can reconstruct the total amount of rock eroded along a river profile as a function of time, $Q_s(t)$, which is given by

$$Q_s(t) = \int_0^L -vA(x)^m \left(\frac{\partial z}{\partial x}\right) \mathrm{d}x \tag{18}$$

where L is the length of a river profile. By integrating these values throughout the Krishna-Godavari drainage system, we predict a sedimentary flux history for this delta. Sedimentary flux calculated in this way provides a minimum estimate since drainage recovery is incomplete and we do not take into account erosion of interfluves, hillslope processes, or variable channel width. Although this calculation inevitably underestimates the true sedimentary flux, the relative changes are probably robust. Model coverage is well-resolved between 50 Ma and the present day but earlier predictions are less certain.

We compare our predicted sedimentary flux with the observed record of *Halkett* [2002] who mapped a grid of regional seismic reflection profiles calibrated with well logs to estimate the volume of solid sediment within the proximal Krishna-Godavari delta as a function of time (Figures 16a and 16b). This record has two prominent peaks in sedimentation. The first one occurs at 70–48 Ma and is associated with regional uplift of the Deccan traps following plume-related rifting between the Seychelles and India. The second one occurs at 23–0 Ma. Clastic deposition dominates during these two pulses of increased sedimentation. The pulses are separated by a 25 Ma period of lower sedimentation where carbonate and mud are the dominant lithologies. This quiescent period correlates with weathering ages of lateritized paleosurfaces that crop out in upland areas. Topographic relief was probably modest since precipitation is inferred to have been significant enough to facilitate pervasive chemical weathering [*Bonnet et al.*, 2014, 2016] (Figure 16c). The first peak cannot be matched since calculated cumulative rock uplift history is poorly resolved pre-50 Ma. However, slow sedimentation from 50 to 25 Ma followed by an increase in sedimentary flux toward the present-

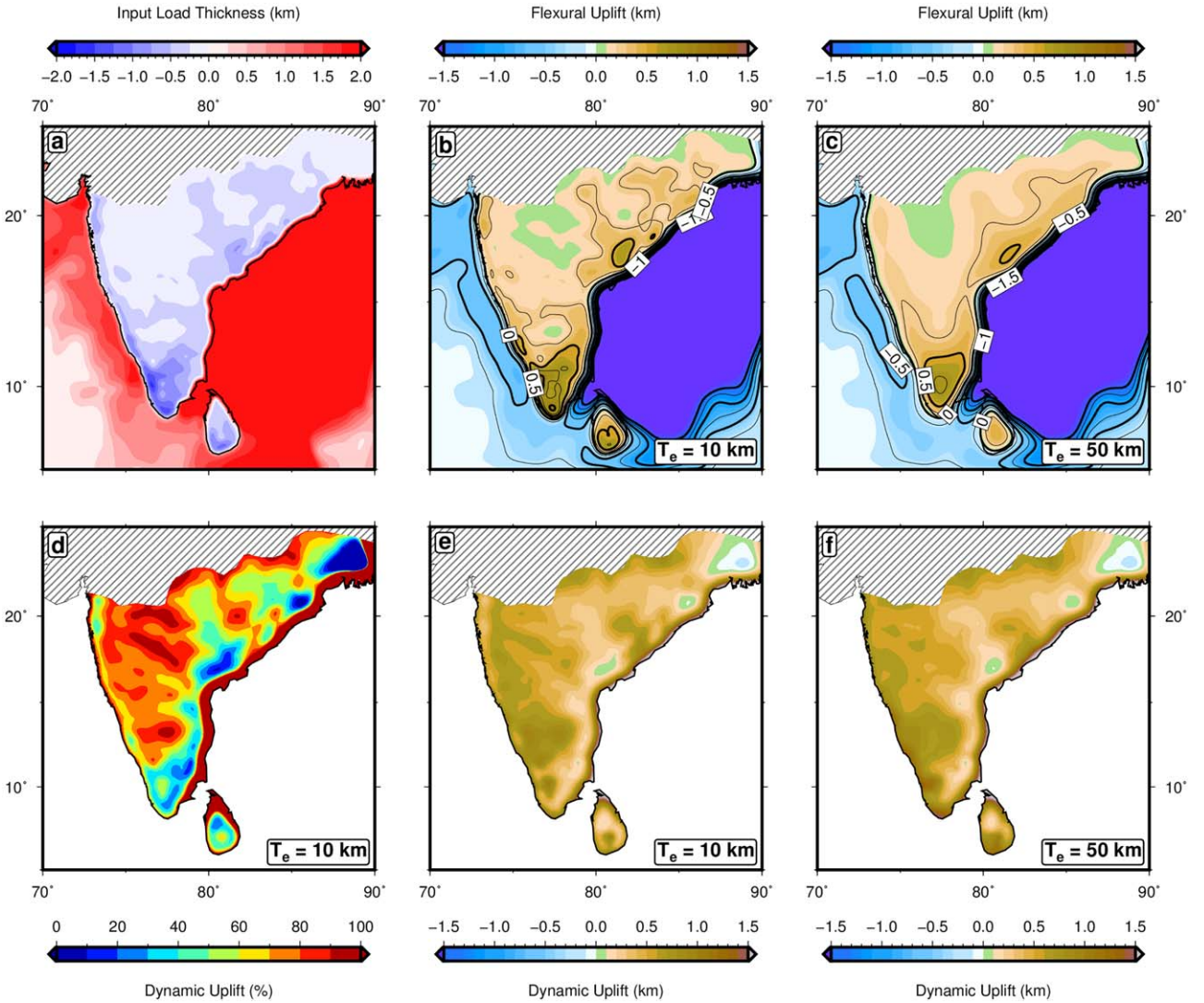

Figure 18. Flexural contributions to uplift over peninsular India. (a) Onshore/offshore load configurations. Onshore load = maximum denudation between 50 and 0 Ma from inverse model (crustal density, ρ_c = 2.7 Mg m^{-3}); offshore load = total sedimentary thickness taken from National Geophysical Data Center (NGDC) grid (average sediment density, $\overline{\rho_s}$ = 2.0 Mg m^{-3}) [*Whittaker et al.*, 2013]. (b) Flexural response to loads for onshore elastic thickness, T_e = 10 km, where T_e of oceanic lithosphere is 20 km. (c) Flexural response to loads for onshore elastic thickness, T_e = 50 km, where T_e of oceanic lithosphere is 20 km. (d) Percentage contribution of nonflexural topographic component where onshore T_e = 10 km. (e) Difference between observed topography and flexural contribution for onshore T_e = 10 km. (f) Difference between observed topography and flexural contribution for onshore T_e = 50 km.

day agrees with the observational record. Spatiotemporal smoothing imposed on the inverse model means that shorter period features observed in the sedimentary record are not accurately matched. Observed and predicted Neogene increases in sedimentation precede monsoon intensification by ~15 Ma, suggesting that rock uplift, and not climate change, is the main driver for increased erosion over the peninsula during Cenozoic times [*An et al.*, 2001].

4.2.4. Offshore Sequence Stratigraphy

The large-scale stratigraphic architecture of surrounding rifted margins provides independent evidence for the existence of Neogene tilting. Along the northwest coast, a regional discontinuity truncates foresets of Lower Miocene to Lower Pliocene strata [*Kumar et al.*, 2009]. The angle of truncation decreases toward the shelf edge, suggesting that this discontinuity records a regional regressive event that occurred after ~16 Ma [*Raju*, 2008] (Figures 17a and 17c). This discontinuity can be mapped onshore up to an elevation of ~150 m. The depth of its offshore extent, corrected for sediment loading, is ~150 m, indicating a relative sea-level fall of at least 300 m. Since there is no evidence for a glacioeustatic drop of this magnitude during that period, it is more plausible that regional uplift of the margin occurred [e.g., *Miller et al.*, 2005].

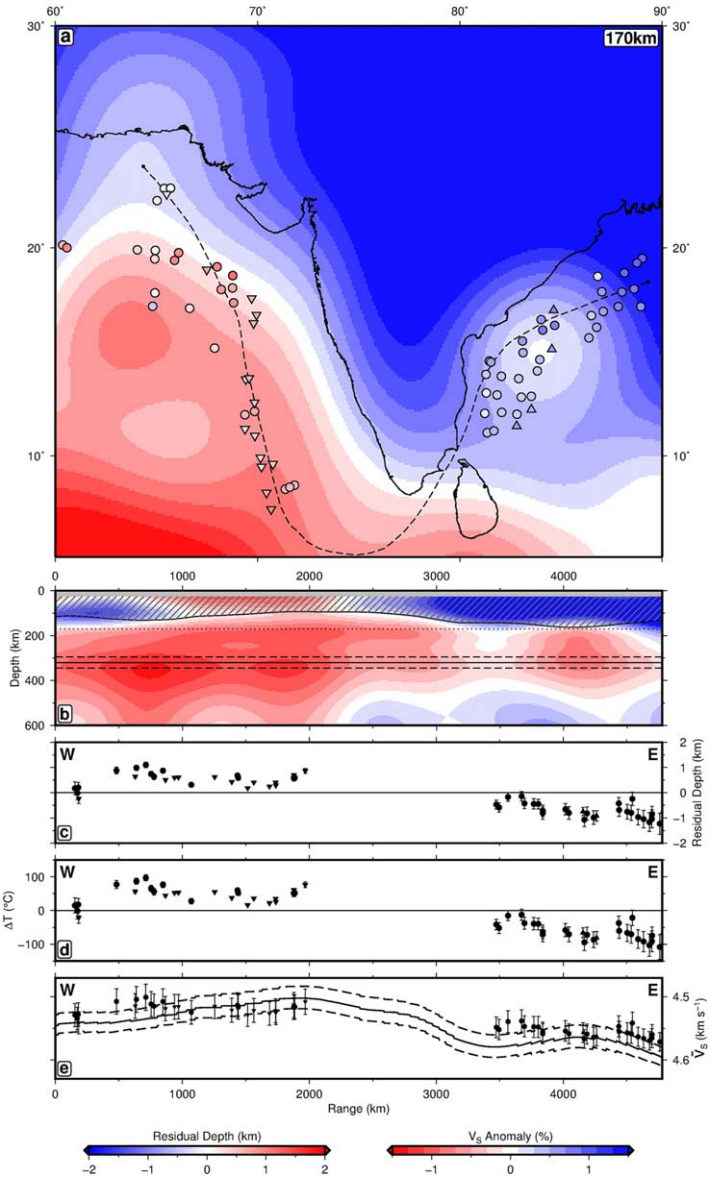

Figure 19. Seismic tomographic model and residual depth anomalies. (a) Horizontal slice through S40RTS model at 170 km depth. Red/blue colors = slow/fast shear wave, V_S, anomalies; colored circles and upward/downward-pointing triangles = water-loaded residual depth measurements; dashed line = path of transect shown in Figures 19b–19e. (b) Vertical slice through S40RTS model along transect. Transparent gray box = oceanic lithosphere [*Priestley and McKenzie*, 2013]; dotted line = depth of horizontal slice shown in Figure 19a; solid/dashed lines = putative base of proposed low viscosity channel at 320 ± 25 km. (c) Residual depth measurements as function of distance along transect. (d) Asthenospheric temperature variation, ΔT, along transect calculated using equation (20) where $h = 200 \pm 25$ km. (e) Solid/dashed lines = shear wave velocity anomalies determined from S40RTS by averaging over putative asthenospheric channel (i.e., 200 ± 25 km); solid circles, upward/downward-pointing triangles = shear wave velocity anomalies calculated from empirical relationship between average ΔT and average V_S for asthenospheric channel; vertical lines = errors estimated from uncertainties in h and T.

Along the east coast, positions of the rollover crests of clinoformal surfaces within a Middle Miocene to Recent sedimentary sequence can be tracked. A switch from progradation to aggradation occurred during Middle Miocene times and is followed by Pleistocene to Holocene retrogradation. This sequence stratigraphic architecture is diagnostic of a rapid increase in accommodation space. By decompacting and unloading the sequence, we estimate that ~600 m of water-loaded subsidence occurred within ~10 Ma (Figures 17b and 17d). Thus a combination of stratigraphic observations are consistent with the inference that Neogene regional tilting of the Indian peninsula is a significant phenomenon.

5. Discussion

Offshore residual depth measurements, inverse modeling of drainage networks and supporting geologic constraints suggest that long-wavelength uplift of the western half of the Indian peninsula has occurred during Neogene times. This inference does not preclude an earlier cycle of Paleocene rock uplift and denudation. We suggest that it is unlikely that active tectonic deformation, crustal isostasy, or plate flexure are responsible for regional eastward tilting. Nevertheless, although combined offshore and onshore tilting is very unlikely to be supported by lithospheric flexure, we acknowledge that, on shorter wavelengths, flexural rigidity can, and probably does, play a role in downwarping the lowland pediment and in maintaining high relief across the rim of the Western Ghats escarpment [*Gilchrist and Summerfield*, 1990; *Whiting et al.*, 1994; *Gunnell and Fleitout*, 1998; *Campanile et al.*, 2008]. We have calculated the flexural effect of combined offshore sedimentary loading and onshore denudational unloading for different values of elastic thickness. Flexural modeling was carried out in the frequency domain using a spectral method with mirrored-edge symmetry [*Watts*, 2001]. A heterogeneous load consisting of the

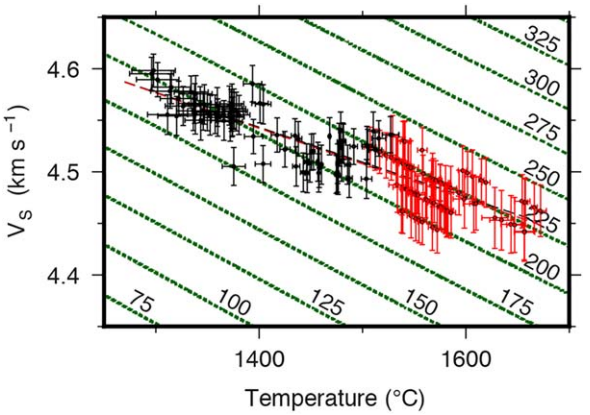

Figure 20. Relationship between shear wave velocity and temperature. Solid circles and crosses = observed empirical relationship between V_S and T with uncertainties that reflect $h = 200 \pm 25$ km; red circles and crosses = $V_{S\text{-}T}$ relationship predicted by parameterization of *Priestley and McKenzie* [2013] for $h = 200 \pm 25$ km; dashed line = best-fitting line to solid circles; red-dashed line = best-fitting line to red circles; green dashed lines = $V_{S\text{-}T}$ relationship predicted for different depths in kilometers from *Priestley and McKenzie* [2013].

offshore distribution of sedimentary deposits and the onshore, post-50 Ma, cumulative denudation determined by inverse modeling was constructed [*Whittaker et al.*, 2013] (Figure 18a). Our results suggest that no more than about 30% of post-50 Ma epeirogenic uplift can be generated by lithospheric flexure, irrespective of the exact value of T_e (Figures 18b–18f).

A more appealing mechanism is a change in the density structure of the lithospheric, or sublithospheric, mantle. The age and duration of regional uplift is incompatible with a progressive decrease in lithospheric density along the western margin since such a decrease would require significant and widespread melt extraction for which there is little evidence [*Turcotte and Emerman*, 1983; *Hawkesworth et al.*, 1990; *Turner and Hawkesworth*, 1995; *Todal and Edholm*, 1999]. Thus, we attribute the observed spatiotemporal rock uplift pattern to convective processes within the sublithospheric mantle.

This inference is supported by earthquake tomographic models (e.g., SMEAN, S40RTS, SL2013sv) and corroborated by receiver function studies. Both indicate the existence of predominantly slow upper mantle shear wave velocity anomalies beneath the western side of the peninsula and fast upper mantle shear wave velocity anomalies beneath the eastern side [*Becker*, 2002; *Ritsema et al.*, 2011; *Mohan et al.*, 2012; *Schaeffer and Lebedev*, 2013]. The planform of this distribution shows good spatial correlation with oceanic residual depth measurements (Figure 19a). Significantly, a band of increased cumulative rock uplift visible in the last time step of the inverse model coincides with the maximum gradient of the shear wave velocity anomaly. This correlation is consistent with expectations about the surficial expression of convective circulation [*Braun et al.*, 2013]. The existence of a low density anomaly within the upper mantle immediately beneath the plate could maintain an west-east dynamic topographic gradient [*Becker and Faccenna*, 2011] (Figures 19b and 19c). Residual depth measurements from the oceanic realm broadly agree with this premise.

It has also been suggested that a low viscosity asthenospheric channel beneath the lithosphere, within which pressure-driven Poiseuille flow occurs, can act to decouple the Earth's surface from convective circulation of the deeper mantle [*Weismüller et al.*, 2015]. The best evidence for the existence of a low viscosity asthenosphere comes from ridge bathymetric, plate motion, glacial rebound, and seismic anisotropic studies [*Buck et al.*, 2009; *Iaffaldano and Bunge*, 2015; *van der Wal et al.*, 2015; *Lin et al.*, 2016]. Low asthenospheric viscosity may be controlled by high temperatures, by partial melting, by the presence of water, or by some combination of all three [*Anderson and Sammis*, 1970; *Karato and Jung*, 1998; *Stixrude and Lithgow-Bertelloni*, 2005]. Above such channels, surface deflections are probably dominated by the effects of thermal buoyancy and, to a lesser extent, by viscous tractions at the lithosphere-asthenosphere boundary [*Robinson et al.*, 1987]. Surface wave dispersion studies of southern India are consistent with the presence of a 180 ± 40 km thick low-velocity layer beneath the lithosphere [*Mitra et al.*, 2008].

Residual depth, z_{res}, as a function of channel thickness, h, and the average temperature deviation, ΔT, is given by

$$z_{res} = \frac{h\alpha\Delta T}{(1-\alpha T_o)} \tag{19}$$

where $\alpha = 3.3\times10^{-5}\,^{\circ}\mathrm{C}^{-1}$ and T_o is the background asthenospheric temperature [*Hartley et al.*, 2011]. For a given channel thickness, we can estimate the average temperature anomaly for each residual depth measurement (Figure 19d). The depth-averaged value of V_S over the thickness of the channel is calculated from

any given tomographic model. This value is used to determine the best-fit linear relationship between V_S and T. The smallest misfit between observed and calculated V_S is obtained for a channel thickness of 200 ± 25 km and a temperature anomaly of ±100 °C (Figure 19e). Note the absence of Neogene volcanism associated with this temperature anomaly which could be cooler if a thicker channel is assumed.

The V_S -T relationship is compared to that predicted by matching surface wave dispersion measurements with a combination of the plate model and continental geothermobarometric constraints [*Priestley and McKenzie*, 2006, 2013]. An optimal fit is obtained for channel thicknesses of 200 ± 25 km using S40RTS [*Ritsema et al*., 2011] (Figure 20). Similar results are obtained using S20RTS, albeit with a larger gradient misfit [*Ritsema et al*., 1999]. An improved fit to the V_S -T gradient is obtained using the SL2013sv tomographic model, although there is a large negative offset in absolute V_S [*Schaeffer and Lebedev*, 2013]. A similarly high offset was recovered for the 3D2015_07Sv model for which the fit to the gradient is less good [*Debayle et al*., 2016]. The larger V_S offset for the SL2013sv and 3D2015_07Sv models probably arises from the different reference velocities used, which are generally slower than for the PREM model at equivalent upper mantle depths. However, gradient misfits may have other possible causes. For example, the parameterization of *Priestley and McKenzie* [2013] is less well resolved below a depth of ~200 km where there is insufficient mantle nodule data to calibrate the V_S -T relationship.

Furthermore, gradient misfits could be caused by the damping function used to stabilize tomographic models. In this instance, V_S variations are oversmoothed, which can give rise to excessively shallow V_S -T gradients. *Takei et al*. [2014] show that the Maxwell time-normalized frequency-attenuation (f'-Q^{-1}) relationship of *McCarthy et al*. [2011] does not apply to the seismic frequency range ($10^8 \leq f' \leq 10^{11}$). Their results show that at high temperatures, for a given f', Q^{-1} will be higher and V_S will be lower than would be predicted by extrapolating the relationship. The anelastic part of the *Priestley and McKenzie* [2013] parameterization will therefore underestimate attenuation at near-solidus temperatures, leading to overestimates of V_S at seismic frequencies and insufficiently steep decreases in V_S as temperatures approach the solidus temperature. Finally, we ignore viscous stresses when relating residual depth anomalies to V_S anomalies. If these forces make a significant contribution, smaller temperature anomalies would be needed for a channel of equivalent thickness, resulting in higher gradient V_S -T relationships that would more closely match those predicted by *Priestley and McKenzie* [2013]. Notwithstanding these complexities, the spatial correlation between residual depth observations and V_S anomaly gradients supports the inference that regional topographic asymmetry is linked to asthenospheric temperature anomalies [*Ritsema et al*., 1999; *Becker*, 2002; *Ritsema et al*., 2011; *Schaeffer and Lebedev*, 2013; *Debayle et al*., 2016].

Many tomographic models show a substantial fast shear wave velocity anomaly within the lower mantle beneath the Indian plate. We suggest that the lack of coherence observed between gravity and topography at wavelengths $>$ 400 km stems from the presence of a deeper-seated density anomaly (Figures 3b and 6c). Topography is mainly sensitive to deflections induced by density variations immediately beneath the base of the plate. In contrast, the long-wavelength gravity field is also affected by density anomalies deeper within the mantle. The large, fast velocity anomaly beneath the Indian Ocean probably represents a positive density anomaly. According to Stokes' flow, this anomaly is expected to be actively sinking and should generate negative deflection of the core-mantle boundary [*Hager and Richards*, 1989; *Steinberger et al*., 2010]. Although this interface is deep, the density contrast across it is large ($\geq$ 4.4 Mg m^{-3}) and deflection of this boundary will have an associated negative gravity anomaly [*Dziewonski and Anderson*, 1981; *Colli et al*., 2016]. This inference is consistent with a flow model suggesting that the presence of this anomaly is consistent with the accumulation of sinking Tethyan slab material [*Nerlich et al*., 2016]. Inferred Neogene rock uplift rates of nearly 0.1 mm a^{-1} and the co-location of residual depth anomalies with shear wave anomalies immediately beneath the lithosphere together suggest that regional tilting of peninsular India and its surrounding oceanic lithosphere is principally maintained by shallow thermal isostasy.

Onset of regional uplift at about 35 Ma across southern India broadly coincides with a major slowdown in plate velocity caused by collision with Eurasia [*Molnar and Stock*, 2009; *Copley et al*., 2010; *Cande and Patriat*, 2015]. We speculate that the speed of northward flow of hot asthenospheric material began to surpass that of the slowing plate above, resulting in the observed northward propagation of regional uplift. This suggestion means that asthenospheric velocity must have exceeded that of the overriding plate throughout Neogene times ($\geq$ 40 mm a^{-1}). Asthenospheric velocities as fast as 400 mm a^{-1} have been documented beneath the North Atlantic Ocean [*Vogt*, 1971; *Hartley et al*., 2011; *Parnell-Turner et al*., 2014]. It is therefore

possible that thermal anomalies in an asthenospheric channel may have progressively impinged from the southwest, following continental collision.

6. Conclusions

To investigate the spatial and temporal pattern of vertical movements of the Indian Peninsula, a combination of offshore and onshore observations are presented and analyzed. Oceanic lithosphere occurs on both sides of India and is characterized by significant residual age-depth anomalies. The asymmetry of these anomalies is consistent with Indian topography. Onshore, the drainage network contains coherent rock uplift signals that are non-linear in space and can be inverted to determine regional uplift histories. We used a stream power formulation to pose a damped linear inverse problem which has enabled 530 longitudinal river profiles to be fitted. The calculated regional rock uplift history suggests that the present-day topography primarily grew during Neogene times.

This history has been calibrated and tested using independent geologic constraints. Prior to ~23 Ma, the development of the eastward tilt was slow, with rock uplift rates along the western margin $\leq$ 0.02 mm a^{-1}. After ~23 Ma uplift rates along the Western Ghats increase rapidly to $\leq$ 0.1 mm a^{-1}. This Neogene increase in uplift is consistent with thermochronologic observations, with sedimentary flux observations and with sequence stratigraphic observations along the continental margins.

This rock uplift history, in conjunction with evidence for modest flexural rigidity and for crustal isostatic anomalies, suggests that the elevated topography of the Western Ghats escarpment is maintained by sublithospheric convective processes. The spatial pattern of regional uplift is consistent with the presence of a slow shear wave velocity anomaly directly beneath the plate. By converting residual depth measurements into depth-averaged temperature anomalies and by comparing these anomalies with the shear wave velocity structure beneath India, we have shown that the size and variation of residual depth anomalies are consistent with a thermal isostatic response to $\pm 100\,^{\circ}C$ temperature variations within a 200 ± 25 km thick asthenospheric channel.

It has not escaped our notice that the specific model we have postulated to account for the generation and maintenance of elevated Indian topography may be applicable to other great escarpments on Earth [*Hoggard et al.*, 2016]. From a broader perspective, the interconnectivity of dynamic topography, landscape development, and offshore stratigraphy described here testifies to the fundamental influence of mantle convection on evolution of the Earth's surface over a range of temporal and spatial scales. By applying integrated methodologies similar to those outlined here, reconstruction of the Cenozoic spatiotemporal pattern of global dynamic topography could be a fruitful endeavor.

Acknowledgments
This research is supported by a collaborative project between BP Exploration and the University of Cambridge. FDR is supported by the NERC. We are grateful to ION Geophysical Corporation for permission to publish seismic reflection images (Figures 2 and 17). We are grateful to D. McKenzie and A.B. Watts for generously sharing their admittance and plate flexure codes with us. We thank P. Bellingham, A. Bump, A. Copley, L. Cowton, D. Lyness, M. Falder, I. Frame, B. Horn, S. Humbert, K. McDermott, R. Parnell-Turner, V. Rodriguez-Tribaldos, J. Rudge, C. Schoonman, and S. Stephenson for their help. M.L. Fox, R.D. Müller, and M. Widdowson provided detailed and insightful reviews. Figures were prepared using Generic Mapping Tools software. The authors declare no competing financial interests. Earth Sciences contribution esc.3757.

References

Acton, C. E., K. Priestley, V. K. Gaur, and S. S. Rai (2010), Group velocity tomography of the Indo-Eurasian collision zone, *J. Geophys. Res.*, *115*, B12335, doi:10.1029/2009JB007021.

Acton, C. E., K. Priestley, S. Mitra, and V. K. Gaur (2011), Crustal structure of the Darjeeling-Sikkim Himalaya and southern Tibet, *Geophys. J. Int.*, *184*(2), 829–852, doi:10.1111/j.1365-246X.2010.04868.x.

Agrawal, P. K., and O. P. Pandey (2004), Unusual lithospheric structure and evolutionary pattern of the cratonic segments of the South Indian shield, *Earth Planets Space*, *56*(2), 139–150.

Ajay, K. K., and A. K. Chaubey (2008), Depth anomalies in the Arabian Basin, NW Indian Ocean, *Geo Mar. Lett.*, *28*, 15–22, doi:10.1007/s00367-007-0085-z.

Alappat, L., M. Frechen, S. Sree Kumar, D. Suresh Babu, R. Ravur, and S. Tsukamoto (2015), Evidence of Late Holocene shoreline progradation in the coast of Kerala, South India obtained from OSL dating of palaeo-beach ridges, *Geomorphology*, *245*, 73–86, doi:10.1016/j.geomorph.2015.05.006.

Ambili, V., and A. Narayana (2014), Tectonic effects on the longitudinal profiles of the Chaliyar River and its tributaries, southwest India, *Geomorphology*, *217*, 37–47, doi:10.1016/j.geomorph. 2014.04.013.

An, Z., J. E. Kutzbach, W. L. Prell, and S. C. Porter (2001), Evolution of Asian monsoons and phased uplift of the Himalaya-Tibetan plateau since Late Miocene times, *Nature*, *411*(6833), 62–66, doi:10.1038/35075035.

Anderson, D. L., and C. Sammis (1970), Partial melting in the upper mantle, *Phys. Earth Planet. Inter.*, *3*, 41–50, doi:10.1016/0031-9201(70)90042-7.

Banerjee, P. (2000), Holocene and Late Pleistocene relative sea level fluctuations along the east coast of India, *Mar. Geol.*, *167*, 243–260, doi:10.1016/S0025-3227(00)00028-1.

Beauvais, A., and D. Chardon (2013), Modes, tempo, and spatial variability of Cenozoic cratonic denudation: The West African example, *Geochem. Geophys. Geosyst.*, *14*, 1590–1608, doi:10.1002/ggge.20093.

Beauvais, A., N. J. Bonnet, D. Chardon, N. Arnaud, and M. Jayananda (2016), Very long-term stability of passive margin escarpment constrained by 40Ar/39Ar dating of K-Mn oxides, *Geology*, *44*(4), 299–302, doi:10.1130/G37303.1.

Becker, J. J., et al. (2009), Global bathymetry and elevation data at 30 arc seconds resolution: SRTM30_PLUS, *Mar. Geod.*, *32*(4), 355–371, doi:10.1080/01490410903297766.
Becker, T. W. (2002), A comparison of tomographic and geodynamic mantle models, *Geochem. Geophys. Geosyst.*, *3*(1), 1003, doi:10.1029/2001GC000168.
Becker, T. W., and C. Faccenna (2011), Mantle conveyor beneath the Tethyan collisional belt, *Earth Planet. Sci. Lett.*, *310*(3-4), 453–461, doi:10.1016/j.epsl.2011.08.021.
Behera, L. (2011), Crustal tomographic imaging and geodynamic implications toward south of Southern Granulite Terrain (SGT), India, *Earth Planet. Sci. Lett.*, *309*(1-2), 166–178, doi:10.1016/j.epsl.2011.04.033.
Bodin, P., and S. Horton (2004), Source parameters and tectonic implications of aftershocks of the Mw 7.6 Bhuj earthquake of 26 January 2001, *Bull. Seismol. Soc. Am.*, *94*(3), 818–827, doi:10.1785/0120030176.
Bonnet, N. J., A. Beauvais, N. Arnaud, D. Chardon, and M. Jayananda (2014), First 40Ar/39Ar dating of intense Late Palaeogene lateritic weathering in Peninsular India, *Earth Planet. Sci. Lett.*, *386*, 126–137, doi:10.1016/j.epsl.2013.11.002.
Bonnet, N. J., A. Beauvais, N. Arnaud, D. Chardon, and M. Jayananda (2016), Cenozoic lateritic weathering and erosion history of peninsular India from 40Ar/39Ar dating of supergene K-Mn oxides, *Chem. Geol.*, *446*, 33–53, doi:10.1016/j.chemgeo.2016.04.018, in press.
Borah, K., S. S. Rai, K. Priestley, and V. K. Gaur (2014), Complex shallow mantle beneath the Dharwar Craton inferred from Rayleigh wave inversion, *Geophys. J. Int.*, *198*(2), 1055–1070, doi:10.1093/gji/ggu185.
Braun, J., X. Robert, and T. Simon-Labric (2013), Eroding dynamic topography, *Geophys. Res. Lett.*, *40*, 1494–1499, doi:10.1002/grl.50310.
Brocher, T. M. (2005), Empirical relations between elastic wavespeeds and density in the Earth's crust, *Bull. Seismol. Soc. Am.*, *95*(6), 2081–2092, doi:10.1785/0120050077.
Broyden, C. G., J. E. Dennis, and J. J. Moré (1973), On the local and superlinear convergence of quasi-Newton methods, *J. Inst. Math Its Appl.*, *12*(3), 223–245, doi:10.1093/imamat/12.3.223.
Brückner, H. (1987), New Data on the Evolution of Konkan (Western Ghats), in *Explorations in the Tropics*, edited by V. S. Datye, pp. 173–184, Prof. K. R. Dikshit Felicitation Volume Comm., Pune.
Brückner, H. (1992), Aspects of weathering and peneplanation in Southern India, *Z. Geomorphol.*, *91*(1), 43–66.
Bruinsma, S. L., C. Förste, O. Abrikosov, J.-M. Lemoine, J.-C. Marty, S. Mulet, M.-H. Rio, and S. Bonvalot (2014), ESA's satellite-only gravity field model via the direct approach based on all GOCE data, *Geophys. Res. Lett.*, *41*, 7508–7514, doi:10.1002/2014GL062045.
Buck, W. R., C. Small, and W. B. F. Ryan (2009), Constraints on asthenospheric flow from the depths of oceanic spreading centers: The East Pacific Rise and the Australian-Antarctic discordance, *Geochem. Geophys. Geosyst.*, *10*, Q09007, doi:10.1029/2009GC002373.
Burckle, L. H. (1989), Distribution of diatoms in sediments of the northern Indian Ocean: Relationship to physical oceanography, *Mar. Micropaleontol.*, *15*(1-2), 53–65, doi:10.1016/0377-8398(89)90004-2.
Campanile, D., C. G. Nambiar, P. Bishop, M. Widdowson, and R. Brown (2008), Sedimentation record in the Konkan-Kerala Basin: Implications for the evolution of the Western Ghats and the Western Indian passive margin, *Basin Res.*, *20*, 3–22, doi:10.1111/j.1365-2117.2007.00341.x.
Campforts, B., and G. Govers (2015), Keeping the edge: A numerical method that avoids knickpoint smearing when solving the stream power law, *J. Geophys. Res. Earth Surf.*, *120*, 1189–1205, doi:10.1002/2014JF003376.
Cande, S. C., and P. Patriat (2015), The anticorrelated velocities of Africa and India in the Late Cretaceous and early Cenozoic, *Geophys. J. Int.*, *200*(1), 227–243, doi:10.1093/gji/ggu392.
Chardon, D., V. Chevillotte, A. Beauvais, G. Grandin, and B. Boulangé (2006), Planation, bauxites and epeirogeny: One or two paleosurfaces on the West African margin?, *Geomorphology*, *82*(3-4), 273–282, doi:10.1016/j.geomorph.2006.05.008.
Chatterjee, S., A. Goswami, and C. R. Scotese (2013), The longest voyage: Tectonic, magmatic, and paleoclimatic evolution of the Indian plate during its northward flight from Gondwana to Asia, *Gondwana Res.*, *23*(1), 238–267, doi:10.1016/j.gr.2012.07.001.
Chaubey, A. K., D. Gopala Rao, K. Srinivas, T. Ramprasad, M. V. Ramana, and V. Subrahmanyam (2002), Analyses of multichannel seismic reflection, gravity and magnetic data along a regional profile across the central-western continental margin of India, *Mar. Geol.*, *182*(3-4), 303–323, doi:10.1016/S0025-3227(01)00241-9.
Clift, P. D. (2010), Enhanced global continental erosion and exhumation driven by Oligo-Miocene climate change, *Geophys. Res. Lett.*, *37*, L09402, doi:10.1029/2010GL043067.
Clift, P. D., and R. A. Plumb (2008), *The Asian Monsoon: Causes, History and Effects*, Cambridge Univ. Press, Cambridge.
Colli, L., S. Ghelichkhan, and H.-P. Bunge (2016), On the ratio of dynamic topography and gravity anomalies in a dynamic Earth, *Geophys. Res. Lett.*, *43*, 2510–2516, doi:10.1002/2016GL067929.
Collier, J. S., V. Sansom, O. Ishizuka, R. N. Taylor, T. A. Minshull, and R. B. Whitmarsh (2008), Age of Seychelles-India break-up, *Earth Planet. Sci. Lett.*, *272*(1-2), 264–277, doi:10.1016/j.epsl.2008. 04.045.
Copley, A., J. P. Avouac, and J. Y. Royer (2010), India-Asia collision and the Cenozoic slowdown of the Indian plate: Implications for the forces driving plate motions, *J. Geophys. Res.*, *115*, B03410, doi:10.1029/2009JB006634.
Copley, A., S. Mitra, R. A. Sloan, S. Gaonkar, and K. Reynolds (2014), Active faulting in apparently stable peninsular India: Rift inversion and a Holocene-age great earthquake on the Tapti Fault, *J. Geophys. Res. Solid Earth*, *119*, 6650–6666, doi:10.1002/2014JB011294.
Cox, K. G. (1989), The role of mantle plumes in the development of continental drainage patterns, *Nature*, *342*(6252), 873–877, doi:10.1038/342873a0.
Cronin, T. (2010), *Paleoclimates: Understanding Climate Change Past and Present*, Columbia Univ. Press, New York.
Crosby, A. G., and D. McKenzie (2009), An analysis of young ocean depth, gravity and global residual topography, *Geophys. J. Int.*, *178*(3), 1198–1219, doi:10.1111/j.1365-246X.2009.04224.x.
Czarnota, K., M. J. Hoggard, N. White, and J. Winterbourne (2013), Spatial and temporal patterns of Cenozoic dynamic topography around Australia, *Geochem. Geophys. Geosyst.*, *14*, 634–658, doi:10.1029/2012GC004392.
Czarnota, K., G. G. Roberts, N. J. White, and S. Fishwick (2014), Spatial and temporal patterns of Australian dynamic topography from River Profile Modeling, *J. Geophys. Res. Solid Earth*, *119*, 1384–1424, doi:10.1002/2013JB010436.
Dalton, C. A., C. H. Langmuir, and A. Gale (2014), Geophysical and geochemical evidence for deep temperature variations beneath mid-ocean ridges, *Science*, *344*(6179), 80–83, doi:10.1126/science. 1249466.
Debayle, E., F. Dubuffet, and S. Durand (2016), An automatically updated S-wave model of the upper mantle and the depth extent of azimuthal anisotropy, *Geophys. Res. Lett.*, *43*, 674–682, doi:10.1002/2015GL067329.
Dodson, M. H. (1973), Closure temperature in cooling geochronological and petrological systems, *Contrib. Mineral. Petrol.*, *40*(3), 259–274, doi:10.1007/BF00373790.
Dziewonski, A. M., and D. L. Anderson (1981), Preliminary reference Earth model, *Phys. Earth Planet. Inter.*, *25*(4), 297–356, doi:10.1016/0031-9201(81)90046-7.

Engdahl, E. R., R. Van der Hilst, and R. Buland (1998), Global teleseismic earthquake relocation with improved travel times and procedures for depth determination, *Bull. Seismol. Soc. Am.*, *88*(3), 722–743.
Food And Agriculture Organization of the United Nations (FAO-UNESCO) (2007), *Digital Soil Map of the World*, version 3.6, Rome, Italy. [Available at http://www.fao.org/geonetwork/srv/en/metadata.show?id=14116.]
Farley, K. A. (2000), Helium diffusion from apatite: General behavior as illustrated by Durango fluorapatite, *J. Geophys. Res.*, *105*(B2), 2903–2914, doi:10.1029/1999JB900348.
Fawcett, P. (1994), The climatic evolution of India and Australia from the Late Permian to mid-Jurassic: A comparison of climate model results with the geologic record, *Geol. Soc. Am. Spec. Pap.*, *288*(1), 139–157.
Förste, C., et al. (2011), EIGEN-6: The new combined global gravity field model including GOCE from the collaboration of GFZ Potsdam and GRGS Toulouse, Abstract G43A-0747 presented at 2011 Fall Meeting, AGU, Washington, D. C.
Fox, C. S. (1923), *The Bauxite and Aluminous Laterite Occurrences of India*, Off. of the Geol. Surv. of India, Calcutta.
Fox, M., L. Goren, D. A. May, and S. D. Willett (2014), Inversion of fluvial channels for paleo-rock uplift rates in Taiwan, *J. Geophys. Res. Earth Surf.*, *119*, 1853–1875, doi:10.1002/2014JF003196.
Ghosh, S., and S. K. Guchhait (2015), Characterization and evolution of primary and secondary laterites in northwestern Bengal Basin, West Bengal, *J. Palaeogeogr.*, *4*(2), 203–230, doi:10.3724/SP.J.1261.2015.00074.
Gilchrist, A. R., and M. A. Summerfield (1990), Differential denudation and flexural isostasy in formation of rifted-margin upwarps, *Nature*, *346*(6286), 739–742, doi:10.1038/346739a0.
Goren, L., S. D. Willett, F. Herman, and J. Braun (2014), Coupled numerical-analytical approach to landscape evolution modeling, *Earth Surf. Processes Landforms*, *39*(4), 522–545, doi:10.1002/esp.3514.
Green, P. F., K. Lidmar-Bergström, P. Japsen, J. M. Bonow, and J. A. Chalmers (2013), Stratigraphic landscape analysis, thermochronology and the episodic development of elevated, passive continental margins, Geol. Surv. Denmark Greenl. Bull., vol. 30, 150 pp., GEUS, Copenhagen, Denmark.
Gunnell, Y. (1997), Relief and climate in south Asia: The influence of the western ghats on the current climate pattern of peninsular India, *Int. J. Climatol.*, *17*(11), 1169–1182, doi:10.1002/(SICI)1097-0088(199709)17:11⟨1169::AID-JOC189⟩3.0.CO;2-W.
Gunnell, Y. (1998), The interaction between geological structure and global tectonics in multistoreyed landscape development: A denudation chronology of the South Indian Shield, *Basin Res.*, *10*(3), 281–310, doi:10.1046/j.1365-2117.1998.00072.x.
Gunnell, Y., and L. Fleitout (1998), Shoulder uplift of the Western Ghats passive margin, India: A denudational model, *Earth Surf. Processes Landforms*, *23*(5), 391–404, doi:10.1002/(SICI) 1096-9837(199805)23:5⟨391::AID-ESP853⟩3.0.CO;2-5.
Gunnell, Y., and D. Harbor (2008), Structural underprint and tectonic overprint in the Angavo (Madagascar) and Western Ghats (India) implications for understanding scarp evolution at passive margins, *J. Geol. Soc. India*, *71*, 763–779.
Gunnell, Y., and D. J. Harbor (2010), Butte detachment: How pre-rift geological structure and drainage integration drive escarpment evolution at rifted continental margins, *Earth Surf. Processes Landforms*, *35*(12), 1373–1385, doi:10.1002/esp.1973.
Gunnell, Y., K. Gallagher, A. Carter, M. Widdowson, and A. J. Hurford (2003), Denudation history of the continental margin of western peninsular India since the early Mesozoic: Reconciling apatite fission-track data with geomorphology, *Earth Planet. Sci. Lett.*, *215*, 187–201, doi:10.1016/S0012-821X(03)00380-7.
Gunnell, Y., R. Braucher, D. Bourlès, and G. André (2007), Quantitative and qualitative insights into bedrock landform erosion on the South Indian craton using cosmogenic nuclides and apatite fission tracks, *Bull. Geol. Soc. Am.*, *119*(5-6), 576–585, doi:10.1130/B25945.1.
Gupta, S., S. S. Rai, K. S. Prakasam, D. Srinagesh, R. K. Chadha, K. Priestley, and V. K. Gaur (2003), First evidence for anomalous thick crust beneath mid-Archean western Dharwar craton, *Curr. Sci.*, *84*(9), 1219–1226.
Hager, B. H., and M. A. Richards (1989), Long-wavelength variations in earth's geoid: Physical models and dynamical implications, *Philos. Trans. R. Soc. A*, *328*(1599), 309–327, doi:10.1098/rsta.1989.0038.
Hager, B. H., R. W. Clayton, M. A. Richards, R. P. Comer, and A. M. Dziewonski (1985), Lower mantle heterogeneity, dynamic topography and the geoid, *Nature*, *313*(6003), 541–545, doi:10.1038/313541a0.
Halkett, A. (2002), Mantle plumes and the sedimentary record: Onshore-offshore India, unpublished PhD dissertation, University of Cambridge, U. K.
Hartley, R. A., G. G. Roberts, N. White, and C. Richardson (2011), Transient convective uplift of an ancient buried landscape, *Nat. Geosci.*, *4*(8), 562–565, doi:10.1038/ngeo1191.
Hawkesworth, C., P. Kempton, N. Rogers, R. Ellam, and P. van Calsteren (1990), Continental mantle lithosphere, and shallow level enrichment processes in the Earth's mantle, *Earth Planet. Sci. Lett.*, *96*(3-4), 256–268, doi:10.1016/0012-821X(90)90006-J.
Hoggard, M. J., N. White, and D. Al-Attar (2016), Global dynamic topography observations reveal limited influence of large-scale mantle flow, *Nat. Geosci.*, *9*, 456–463, doi:10.1038/ngeo2709.
Howard, A. D., and G. Kerby (1983), Channel changes in badlands, *Geol. Soc. Am. Bull.*, *94*(6), 739–752, doi:10.1130/0016-7606(1983)94⟨739:CCIB⟩2.0.CO;2.
Iaffaldano, G., and H.-P. Bunge (2015), Rapid plate motion variations through geological time: Observations serving geodynamic interpretation, *Annu. Rev. Earth Planet. Sci.*, *43*(1), 571–592, doi:10.1146/annurev-earth-060614-105117.
Iaffaldano, G., L. Husson, and H. P. Bunge (2011), Monsoon speeds up Indian plate motion, *Earth Planet. Sci. Lett.*, *304*(3-4), 503–510, doi:10.1016/j.epsl.2011.02.026.
Jagadeesh, S., and S. S. Rai (2008), Thickness, composition, and evolution of the Indian Precambrian crust inferred from broadband seismological measurements, *Precambrian Res.*, *162*, 4–15, doi:10.1016/j.precamres.2007.07.009.
Julià, J., S. Jagadeesh, S. S. Rai, and T. J. Owens (2009), Deep crustal structure of the Indian shield from joint inversion of P wave receiver functions and Rayleigh wave group velocities: Implications for Precambrian crustal evolution, *J. Geophys. Res.*, *114*, B10313, doi:10.1029/2008JB006261.
Kaila, K. (1979), Crustal structure along Kavali-Udipi profile in the Indian Peninsular Shield from deep seismic sounding, *J. Geol. Soc. India*, *20*(7), 307–333.
Kaila, K., P. Murty, V. Rao, and G. Kharetchko (1981), Crustal structure from deep seismic soundings along the Koyna II (Kelsi-Loni) profile in the Deccan Trap area, India, *Tectonophysics*, *73*(4), 365–384, doi:10.1016/0040-1951(81)90223-7.
Kailasam, L. N. (1975), Epeirogenic studies in India with reference to recent vertical movements, *Tectonophysics*, *29*, 505–521, doi:10.1016/0040-1951(75)90178-X.
Kalaswad, S., M. K. Roden, D. S. Miller, and M. Morisawa (1993), Evolution of the continental margin of western India: New evidence from apatite fission-track dating, *J. Geol.*, *101*(5), 667–673, doi:10.1086/648258.
Kale, V. S., and K. V. Subbarao (2004), Some observations on the recession of the Western Ghat escarpment in the Deccan Trap Region, India: Based on geomorphological evidence, *Trans. Japanese Geomorphol. Union*, *25*(3), 231–245.

Kale, V. S., S. Sengupta, H. Achyuthan, and M. K. Jaiswal (2014), Tectonic controls upon Kaveri River drainage, cratonic Peninsular India: Inferences from longitudinal profiles, morphotectonic indices, hanging valleys and fluvial records, *Geomorphology*, *227*, 153–165, doi:10.1016/j.geomorph.2013.07.027.

Karato, S.-i., and H. Jung (1998), Water, partial melting and the origin of the seismic low velocity and high attenuation zone in the upper mantle, *Earth Planet. Sci. Lett.*, *157*(34), 193–207, doi:10.1016/S0012-821X(98)00034-X.

Kaula, W. M. (1963), Tesseral harmonics of the gravitational field and geodetic datum shifts derived from camera observations of satellites, *J. Geophys. Res.*, *68*(2), 473–494.

Kayal, J. R., V. K. Srivastava, P. Kumar, R. Chatterjee, and P. K. Khan (2011), Evaluation of crustal and upper mantle structures using receiver function analysis: ISM broadband observatory data, *J. Geol. Soc. India*, *78*(1), 76–80, doi:10.1007/s12594-011-0069-5.

Keller, G., S. C. Khosla, R. Sharma, A. Khosla, S. Bajpai, and T. Adatte (2009), Early Danian planktic foraminifera from cretaceous-tertiary intertrappean beds At Jhilmili, Chhindwara District, Madhya Pradesh, India, *J. Foraminifer. Res.*, *39*(1), 40–55, doi:10.2113/gsjfr.39.1.40.

Kench, P. S., S. G. Smithers, R. F. McLean, and S. L. Nichol (2009), Holocene reef growth in the Maldives: Evidence of a mid-Holocene sea-level high stand in the central Indian Ocean, *Geology*, *37*(5), 455–458, doi:10.1130/G25590A.1.

Kent, D. V., and G. Muttoni (2008), Equatorial convergence of India and early Cenozoic climate trends., *Proc. Natl. Acad. Sci. U. S. A.*, *105*(42), 16,065–16,070, doi:10.1073/pnas.0805382105.

Kern, A. K., M. Harzhauser, M. Reuter, A. Kroh, and W. E. Piller (2013), The Miocene coastal vegetation of southwestern India and its climatic significance, *Palaeoworld*, *22*(3-4), 119–132, doi:10.1016/j.palwor.2013.10.001.

Ketcham, R. A. (2005), Forward and inverse modeling of low-temperature thermochronometry data, *Rev. Mineral. Geochem.*, *58*(1), 275–314, doi:10.2138/rmg.2005.58.11.

Knight, K. B., P. R. Renne, A. Halkett, and N. White (2003), 40Ar/39Ar dating of the Rajahmundry Traps, Eastern India and their relationship to the Deccan Traps, *Earth Planet. Sci. Lett.*, *208*(1-2), 85–99, doi:10.1016/S0012-821X(02)01154-8.

Kroon, D., T. Steens, S. R. Troelstra, and U. Kingdom (1991), Onset of monsoonal related upwelling in the western Arabian sea as revealed by planktonic foraminifers, *Proc. Ocean Drill. Program, Sci. Results*, *117*(13), 257–263.

Kumar, N., H. Zeyen, A. P. Singh, and B. Singh (2013), Lithospheric structure of southern Indian shield and adjoining oceans: Integrated modelling of topography, gravity, geoid and heat flow data, *Geophys. J. Int.*, *194*(1), 30–44, doi:10.1093/gji/ggt080.

Kumar, P., P. K. Saraswati, and S. Banerjee (2009), Early Miocene shell concentration in the mixed carbonate-siliciclastic system of Kutch and their distribution in sequence stratigraphic framework, *J. Geol. Soc. India*, *74*(4), 432–444, doi:10.1007/s12594-009-0158-x.

Kumar, P., M. Ravi Kumar, G. Srijayanthi, K. Arora, D. Srinagesh, R. K. Chadha, and M. K. Sen (2013), Imaging the lithosphere-asthenosphere boundary of the Indian plate using converted wave techniques, *J. Geophys. Res. Solid Earth*, *118*, 5307–5319, doi:10.1002/jgrb.50366.

Kumaran, K. P. N., M. Shindikar, and R. B. Limaye (2004), Mangrove associated lignite beds of Malvan, Konkan: Evidence for higher sea-level during the Late Tertiary (Neogene) along the west coast of India, *Curr. Sci.*, *86*(2), 335–340.

Lin, P.-Y. P., J. B. Gaherty, G. Jin, J. A. Collins, D. Lizarralde, R. L. Evans, and G. Hirth (2016), High-resolution seismic constraints on flow dynamics in the oceanic asthenosphere, *Nature*, *535*(7613), 538–541, doi:10.1038/nature18012.

Lisker, F., B. Ventura, and U. A. Glasmacher (2009), Apatite thermochronology in modern geology, *Geol. Soc. Spec. Publ.*, *324*(1), 1–23, doi:10.1144/SP324.1.

Luke, J. C. (1972), Mathematical models for landform evolution, *J. Geophys. Res.*, *77*(14), 2460–2464, doi:10.1029/JB077i014p02460.

Luke, J. C. (1974), Special solutions for nonlinear erosion problems, *J. Geophys. Res.*, *79*(26), 4035–4040, doi:10.1029/JB079i026p04035.

Luke, J. C. (1976), A note on the use of characteristics in slope evolution models, *Z. Geomorph. Supp.*, *25*, 114–119.

Maceira, M., and C. J. Ammon (2009), Joint inversion of surface wave velocity and gravity observations and its application to central Asian basins shear velocity structure, *J. Geophys. Res. Solid Earth*, *114*, *B02314*, doi:10.1029/2007JB005157.

Mandal, P. (2012), Passive-source seismic imaging of the crust and upper mantle beneath the 2001 Mw 7.7 Bhuj earthquake region, Gujarat, India, *Bull. Seismol. Soc. Am.*, *102*(1), 252–266, doi:10.1785/0120110116.

Mandal, S. K., M. G. Fellin, J.-P. Burg, and C. Maden (2015a), Phanerozoic surface history of southern Peninsular India from apatite (U/Th-Sm)/He data, *Geochem. Geophys. Geosyst.*, *16*, 3626–3648, doi:10.1002/2015GC005977.

Mandal, S. K., M. Lupker, J.-P. Burg, P. G. Valla, N. Haghipour, and M. Christl (2015b), Spatial variability of ^{10}Be-derived erosion rates across the southern Peninsular Indian escarpment: A key to landscape evolution across passive margins, *Earth Planet. Sci. Lett.*, *425*, 154–167, doi:10.1016/j.epsl.2015.05.050.

Mandal, S. K., J.-P. Burg, and N. Haghipour (2016), Geomorphic fluvial markers reveal transient landscape evolution in tectonically quiescent southern Peninsular India, *Geol. J.*, doi:10.1002/gj.2833.

McCarthy, C., Y. Takei, and T. Hiraga (2011), Experimental study of attenuation and dispersion over a broad frequency range: 2. The universal scaling of polycrystalline materials, *J. Geophys. Res.*, *116*, *B09207*, doi:10.1029/2011JB008384.

McKenzie, D. (2003), Estimating *Te* in the presence of internal loads, *J. Geophys. Res.*, *108*(B9), 2438, doi:10.1029/2002JB001766.

McKenzie, D. (2016), A note on estimating *Te* from Bouguer coherence, *GEM—Int. J. Geomath.*, *7*(1), 103–116, doi:10.1007/s13137-015-0078-4.

McKenzie, D., and D. Fairhead (1997), Estimates of the effective elastic thickness of the continental lithosphere from Bouguer and free air gravity anomalies, *J. Geophys. Res.*, *102(*B12*)*, 27,523–27,552, doi:1029/97JB02481.

McKenzie, D., W. Yi, and R. Rummel (2015), Estimates of *Te* for continental regions using GOCE gravity, *Earth Planet. Sci. Lett.*, *428*, 97–107, doi:10.1016/j.epsl.2015.07.036.

Meher-Homji, V. M. (1989), History of vegetation of peninsular India, *Man Environ.*, *13*(1), 1–10.

Meyer, D. J., T. Tachikawa, M. Abrams, H. Tsu, M. Hato, D. B. Gesch, and R. E. Crippen (2011), The ASTER Global Digital Elevation Model version 2.0 - Early Validation Results, American Geophysical Union Fall Meeting 2011, abstract IN43B-1442, San Francisco.

Miller, K. G., M. A. Kominz, J. V. Browning, J. D. Wright, G. S. Mountain, M. E. Katz, P. J. Sugarman, B. S. Cramer, N. Christie-Blick, and S. F. Pekar (2005), The Phanerozoic record of global sea-level change., *Science*, *310*, 1293–1298, doi:10.1126/science.1116412.

Mishra, D. C., G. Laxman, and K. Arora (2004), Large-wavelength gravity anomalies over the Indian continent: Indicators of lithospheric flexure and uplift and subsidence of Indian Peninsular Shield related to isostasy, *Curr. Sci.*, *86*, 861–867.

Mitra, S., S. N. Bhattacharya, and S. K. Nath (2008), Crustal structure of the Western Bengal basin from joint analysis of teleseismic receiver functions and Rayleigh-wave dispersion, *Bull. Seismol. Soc. Am.*, *98*(6), 2715–2723, doi:10.1785/0120080141.

Mohan, G., M. R. Kumar, D. Saikia, K. A. P. Kumar, P. K. Tiwari, and G. Surve (2012), Imprints of volcanism in the upper mantle beneath the NW Deccan volcanic province, *Lithosphere*, *4*, 150–159, doi:10.1130/L178.1.

Molnar, P., and J. M. Stock (2009), Slowing of India's convergence with Eurasia since 20 Ma and its implications for Tibetan mantle dynamics, *Tectonics*, *28*, TC3001, doi:10.1029/2008TC002271.

Montgomery, D. R., and W. E. Dietrich (1988), Where do channels begin?, *Nature*, *336*(6196), 232–234, doi:10.1038/336232a0.

Mouthereau, F., A. B. Watts, and E. Burov (2013), Structure of orogenic belts controlled by lithosphere age, *Nat. Geosci.*, *6*(8), 1–5, doi:10.1038/ngeo1902.
Müller, R. D., M. Sdrolias, C. Gaina, and W. R. Roest (2008), Age, spreading rates, and spreading asymmetry of the world's ocean crust, *Geochem. Geophys. Geosyst.*, *9*, Q04006, doi:10.1029/2007GC001743.
Müller, R. D. D., V. Yatheesh, and M. Shuhail (2015), The tectonic stress field evolution of India since the Oligocene, *Gondwana Res.*, *28*(2), 612–624, doi:10.1016/j.gr.2014.05.008.
Nair, V. G. (2006), Impact of Western Ghats orography on the weather and climate over southern Peninsular India: A mesoscale modelling study, PhD dissertation, University of Science and Technology, Cochin, India.
Nerlich, R., L. Colli, S. Ghelichkhan, B. Schuberth, and H.-P. Bunge (2016), Constraining central Neo-Tethys Ocean reconstructions with mantle convection models, *Geophys. Res. Lett.*, *43*, 9595–9603, doi:10.1002/2016GL070524.
Newton, R. C., and E. C. Hansen (1986), The South India-Sri Lanka high-grade terrain as a possible deep-crust section, *Geol. Soc. Spec. Publ.*, *24*(1), 297–307, doi:10.1144/GSL.SP.1986.024.01.26.
Panasyuk, S. V., and B. H. Hager (2000), Models of isostatic and dynamic topography, geoid anomalies, and their uncertainties, *J. Geophys. Res.*, *105*(B12), 28,199–28,209, doi:10.1029/2000JB900249.
Pandey, O. P., P. K. Agrawal, and J. G. Negi (1996), Evidence of low density sub-crustal underplating beneath western continental region of India and adjacent Arabian Sea: Geodynamical considerations, *J. Geodyn.*, *21*(4), 365–377, doi:10.1016/0264-3707(95)00036-4.
Parker, R. L. (1994), *Geophysical Inverse Theory*, Princeton Univ. Press, Princeton, N. J.
Parnell-Turner, R., N. White, T. Henstock, B. Murton, J. Maclennan, and S. M. Jones (2014), A continuous 55-million-year record of transient mantle plume activity beneath Iceland, *Nat. Geosci.*, *7*(12), 914–919, doi:10.1038/ngeo2281.
Pathak, A., M. Ravi Kumar, and D. Sarkar (2006), Seismic structure of Sri Lanka using receiver function analysis: A comparison with other high-grade Gondwana terrains, *Gondwana Res.*, *10*(1-2), 198–202, doi:10.1016/j.gr.2005.10.006.
Paul, J. D., G. G. Roberts, and N. White (2014), The African landscape through space and time, *Tectonics*, *33*, 898–935, doi:10.1002/2013TC003479.
Pedoja, K., et al. (2011), Relative sea-level fall since the last interglacial stage: Are coasts uplifting worldwide?, *Earth Sci. Rev.*, *108*(1-2), 1–15, doi:10.1016/j.earscirev.2011.05.002.
Powar, K. B. (1993), Geomorphological evolution of Konkan Coastal Belt and adjoining Sahyadri Uplands with reference to Quaternary uplift, *Curr. Sci.*, *64*(11-12), 793–796.
Praveen Kumar, K., and G. Mohan (2014), Crustal velocity structure beneath Saurashtra, NW India, through waveform modeling: Implications for magmatic underplating, *J. Asian Earth Sci.*, *79*, 173–181, doi:10.1016/j.jseaes.2013.09.006.
Priestley, K., and D. McKenzie (2006), The thermal structure of the lithosphere from shear wave velocities, *Earth Planet. Sci. Lett.*, *244*, 285–301, doi:10.1016/j.epsl.2006.01.008.
Priestley, K., and D. McKenzie (2013), The relationship between shear wave velocity, temperature, attenuation and viscosity in the shallow part of the mantle, *Earth Planet. Sci. Lett.*, *381*, 78–91, doi:10.1016/j.epsl.2013.08.022.
Pritchard, D., G. G. Roberts, N. J. White, and C. N. Richardson (2009), Uplift histories from river profiles, *Geophys. Res. Lett.*, *36*, L24301, doi:10.1029/2009GL040928.
Radakrishna, B. P. (1991), Neogene uplift and geomorphic rejuvenation of the Indian Peninsula, *Curr. Sci.*, *64*(11-12), 787–793.
Radakrishna, B. P. (1992), Evolution of river Cauvery: A point of view, *Curr. Sci.*, *63*(7), 348–353.
Rai, A., V. K. Gaur, S. S. Rai, and K. Priestley (2009), Seismic signatures of the Pan-African orogeny: Implications for southern Indian high-grade terranes, *Geophys. J. Int.*, *176*(2), 518–528, doi:10.1111/j.1365-246X.2008.03965.x.
Rai, S. S. (2003), Crustal shear velocity structure of the south Indian shield, *J. Geophys. Res.*, *108*(B2), 2088, doi:10.1029/2002JB001776.
Rai, S. S., T. V. Kumar, and S. Jagadeesh (2005), Seismic evidence for significant crustal thickening beneath Jabalpur earthquake, 21 May 1997, source region in Narmada-Son lineament, central India, *Geophys. Res. Lett.*, *32*, L22306, doi:10.1029/2005GL023580.
Rai, S. S., K. Borah, R. Das, S. Gupta, S. Srivastava, K. S. Prakasam, K. Sivaram, S. Kumar, and R. Meena (2013), The South India Precambrian crust and shallow lithospheric mantle: Initial results from the India Deep Earth Imaging Experiment (INDEX), *J. Earth Syst. Sci.*, *122*(6), 1435–1453, doi:10.1007/s12040-013-0357-0.
Raju, D. S. N. (2008), Stratigraphy of India, *ONGC Bull. Spec. Issue*, *43*(1), 44.
Rao, K. M., M. R. Kumar, and B. K. Rastogi (2015), Crust beneath the Northwestern Deccan Volcanic Province, India: Evidence for uplift and magmatic underplating, *J. Geophys. Res. Solid Earth*, *120*, 3385–3405, doi:10.1002/2014JB011819.
Ravi Kumar, M., J. Saul, D. Sarkar, R. Kind, and A. K. Shukla (2001), Crustal structure of the Indian Shield: New constraints from teleseismic receiver functions, *Geophys. Res. Lett.*, *28*(7), 1339–1342, doi:10.1029/2000GL012310.
Reddy, P. R. (2005), Crustal velocity structure of western India and its use in understanding intraplate seismicity, *Curr. Sci.*, *88*(10), 1652–1657.
Reuter, M., W. E. Piller, M. Harzhauser, and A. Kroh (2013), Cyclone trends constrain monsoon variability during late Oligocene sea level highstands (Kachchh Basin, NW India), *Clim. Past*, *9*, 2101–2115, doi:10.5194/cp-9-2101-2013.
Ritsema, J., H. J. van Heijst, and J. H. Woodhouse (1999), Complex Shear Wave Velocity Structure Imaged Beneath Africa and Iceland, *Science*, *286*(5446), 1925–1928, doi:10.1126/science.286.5446.
Ritsema, J., A. Deuss, H. J. Van Heijst, and J. H. Woodhouse (2011), S40RTS: A degree-40 shear-velocity model for the mantle from new Rayleigh wave dispersion, teleseismic travel time and normal-mode splitting function measurements, *Geophys. J. Int.*, *184*, 1223–1236, doi:10.1111/j.1365-246X.2010.04884.x.
Roberts, G. G., and N. White (2010), Estimating uplift rate histories from river profiles using African examples, *J. Geophys. Res.*, *115*, B02406, doi:10.1029/2009JB006692.
Roberts, G. G., N. J. White, G. L. Martin-Brandis, and A. G. Crosby (2012), An uplift history of the Colorado Plateau and its surroundings from inverse modeling of longitudinal river profiles, *Tectonics*, *31*, TC4022, doi:10.1029/2012TC003107.
Robinson, E. M., B. Parsons, and S. F. Daly (1987), The effect of a shallow low viscosity zone on the apparent compensation of mid-plate swells, *Earth Planet. Sci. Lett.*, *82*(3), 335–348, doi:10.1016/0012-821X(87)90207-X.
Rosenbloom, N. A., and R. S. Anderson (1994), Hillslope and channel evolution in a marine terraced landscape, Santa Cruz, California, *J. Geophys. Res.*, *99*(B7), 14,013–14,029, doi:10.1029/94JB00048.
Roy, S., and R. U. M. Rao (2000), Heat flow in the Indian, *J. Geophys. Res.*, *105*(B11), 587–625, doi:10.1029/2000JB900257.
Rudge, J. F., G. G. Roberts, N. J. White, and C. N. Richardson (2015), Uplift histories of Africa and Australia from linear inverse modeling of drainage inventories, *J. Geophys. Res. Earth Surf.*, *120*, 894–914, doi:10.1002/2014JF003297.

Sahu, H. S., M. J. Raab, B. P. Kohn, A. J. W. Gleadow, and D. Kumar (2013), Denudation history of Eastern Indian peninsula from apatite fission track analysis: Linking possible plume-related uplift and the sedimentary record, *Tectonophysics*, *608*, 1413–1428, doi:10.1016/j.tecto.2013.06.002.
Sandwell, D. T., R. D. Muller, W. H. F. Smith, E. Garcia, and R. Francis (2014), New global marine gravity model from CryoSat-2 and Jason-1 reveals buried tectonic structure, *Science*, *346*(6205), 65–67, doi:10.1126/science.1258213.
Sarkar, D., M. R. Kumar, J. Saul, R. Kind, P. S. Raju, R. K. Chadha, and A. K. Shukla (2003), A receiver function perspective of the Dharwar craton (India) crustal structure, *Geophys. J. Int.*, *154*(1), 205–211, doi:10.1046/j.1365-246X.2003.01970.x.
Saul, J., M. R. Kumar, and D. Sarkar (2000), Lithospheric and upper mantle structure of the Indian Shield, from teleseismic receiver functions, *Geophys. Res. Lett.*, *27*(16), 2357–2360, doi:10.1029/1999GL011128.
Schaeffer, A. J., and S. Lebedev (2013), Global shear speed structure of the upper mantle and transition zone, *Geophys. J. Int.*, *194*(1), 417–449, doi:10.1093/gji/ggt095.
Schmidt, P., V. Prasad, and P. Ramam (1983), Magnetic ages of some Indian laterites, *Palaeogeogr. Palaeoclimatol. Palaeoecol.*, *44*(3-4), 185–202, doi:10.1016/0031-0182(83)90102-5.
Sheth, H. (2007), Plume-related regional pre-volcanic uplift in the Deccan Traps: Absence of evidence, evidence of absence, *Geol. Soc. Am. Spec. Pap.*, *430*(1), 785–813.
Shukla, A., R. C. Mehrotra, R. A. Spicer, T. E. Spicer, and M. Kumar (2014), Cool equatorial terrestrial temperatures and the South Asian monsoon in the Early Eocene: Evidence from the Gurha Mine, Rajasthan, India, *Palaeogeogr. Palaeoclimatol. Palaeoecol.*, *412*, 187–198, doi:10.1016/j.palaeo.2014.08.004.
Siddall, M., E. J. Rohling, A. Almogi-Labin, C. Hemleben, D. Meischner, I. Schmelzer, and D. A. Smeed (2003), Sea-level fluctuations during the last glacial cycle., *Nature*, *423*(6942), 853–858, doi:10.1038/nature01690.
Siddall, M., E. Bard, E. J. Rohling, and C. Hemleben (2006), Sea-level reversal during termination II, *Geology*, *34*(10), 817–820, doi:10.1130/G22705.1.
Singh, A., B. K. Misra, B. D. Singh, and G. K. B. Navale (1992), The Neyveli lignite deposits (Cauvery basin), India: Organic composition, age and depositional pattern, *Int. J. Coal Geol.*, *21*(1-2), 45–97, doi:10.1016/0166-5162(92)90035-U.
Singh, A., M. R. Kumar, N. Kumar, D. Saikia, P. Solomon Raju, D. Srinagesh, N. P. Rao, and D. Sarkar (2012), Seismic signatures of an altered crust and a normal transition zone structure beneath the Godavari rift, *Precambrian Res.*, *220-221*, 1–8, doi:10.1016/j.precamres.2012.07.006.
Singh, A., C. Singh, and B. L. N. Kennett (2015), A review of crust and upper mantle structure beneath the Indian subcontinent, *Tectonophysics*, *644-645*, 1–21, doi:10.1016/j.tecto.2015.01.007.
Singh, A. D. (1998), Early-middle Miocene Planktic foraminifera from the quilon formation, Kerala, *Geol. Soc. India*, *52*(3), 313–316.
Sklar, D. W. E. (2001), Sediment and rock strength controls on river incision into bedrock, *Geology*, *29*(12), 1087–1090, doi:10.1130/0091-7613(2001)029⟨1087:SARSCO⟩2.0.CO.
Sklar, L., and W. E. Dietrich (1998), Rivers over rock: Fluvial processes in bedrock channels, *Geophys. Monogr. Ser.*, *107*, 237–260, doi:10.1029/GM107.
Stein, C. A., and S. Stein (1992), A model for the global variation in oceanic depth and heat flow with lithospheric age, *Nature*, *356*, 133–135.
Steinberger, B., S. C. Werner, and T. H. Torsvik (2010), Deep versus shallow origin of gravity anomalies, topography and volcanism on Earth, Venus and Mars, *Icarus*, *207*(2), 564–577, doi:10.1016/j.icarus.2009.12.025.
Stephenson, S. N., G. G. Roberts, M. J. Hoggard, and A. C. Whittaker (2014), A Cenozoic uplift history of Mexico and its surroundings from longitudinal river profiles, *Geochem. Geophys. Geosyst.*, *15*, 4734–4758, doi:10.1002/2014GC005425.
Stixrude, L., and C. Lithgow-Bertelloni (2005), Thermodynamics of mantle minerals I. Physical properties, *Geophys. J. Int.*, *162*(2), 610–632, doi:10.1111/j.1365-246X.2005.02642.x.
Stock, J. D., and D. R. Montgomery (1999), Geologic constraints on bedrock river incision using the stream power law, *J. Geophys. Res.*, *104*(B3), 4983–4993, doi:10.1029/98JB02139.
Suryawanshi, R. A., and R. B. Golekar (2014), Geochemistry of sub-surface Tertiary: Sediments of Ratnagiri District, Maharashtra, India, *Int. J. Adv. Earth Sci.*, *3*(1), 1–12.
Takei, Y., F. Karasawa, and H. Yamauchi (2014), Temperature, grain size, and chemical controls on polycrystal anelasticity over a broad frequency range extending into the seismic range, *J. Geophys. Res. Solid Earth*, *119*, 5414–5443, doi:10.1002/2014JB011146.
Tapley, B., J. Ries, S. Bettadpur, D. Chambers, M. Cheng, F. Condi, and S. Poole (2007), The GGM03 mean earth gravity model from GRACE, *EOS Trans. AGU*, 88(52), Fall Meet. Suppl., Abstract G42A-03.
Tarboton, D. G. (1997), A new method for the determination of flow directions and upslope areas in grid digital elevation models, *Water Resour. Res.*, *33*(2), 309–319, doi:10.1029/96WR03137.
Tawde, S. A., and C. Singh (2015), Investigation of orographic features influencing spatial distribution of rainfall over the Western Ghats of India using satellite data, *Int. J. Climatol.*, *35*(9), 2280–2293, doi:10.1002/joc.4146.
Thorne, R. L., S. Roberts, and R. Herrington (2012), Climate change and the formation of nickel laterite deposits, *Geology*, *40*(4), 331–334, doi:10.1130/G32549.1.
Tiwari, P. K., G. Surve, and G. Mohan (2006), Crustal constraints on the uplift mechanism of the Western Ghats of India, *Geophys. J. Int.*, *167*(3), 1309–1316, doi:10.1111/j.1365-246X.2006. 03093.x.
Todal, A., and O. Edholm (1999), Continental margin off Western India and Deccan Large Igneous Province, *Mar. Geophys. Res.*, (1995), 273–291.
Tomkin, J. H. (2003), Quantitative testing of bedrock incision models for the Clearwater River, NW Washington State, *J. Geophys. Res.*, *108*(B6), 2308, doi:10.1029/2001JB000862.
Turcotte, D. L., and S. H. Emerman (1983), Mechanisms of active and passive rifting, *Tectonophysics*, *94*(1-4), 39–50, doi:10.1016/0040-1951(83)90008-2.
Turner, S., and C. Hawkesworth (1995), The nature of the sub-continental mantle: Constraints from the major-element composition of continental flood basalts, *Chem. Geol.*, *120*(3-4), 295–314, doi:10.1016/0009-2541(94)00143-V.
Valdiya, K. S. (2001), Tectonic resurgence of the Mysore plateau and surrounding regions in cratonic Southern India, *Curr. Sci.*, *81*(8), 1068–1089.
Valeton, I. (1983), Palaeoenvironment of lateritic bauxites with vertical and lateral differentiation, *Geol. Soc. Spec. Publ.*, *11*(1), 77–90, doi:10.1144/gsl.sp.1983.011.01.10.
Van Bocxlaer, I., S. Biju, S. P. Loader, and F. Bossuyt (2009), Toad radiation reveals into-India dispersal as a source of endemism in the Western Ghats-Sri Lanka biodiversity hotspot, *BMC Evol. Biol.*, *9*(1), 131, doi:10.1186/1471-2148-9-131.
van der Beek, P., and P. Bishop (2003), Cenozoic river profile development in the Upper Lachlan catchment (SE Australia) as a test of quantitative fluvial incision models, *J. Geophys. Res.*, *108*(B6), 2309, doi:10.1029/2002JB002125.

van der Wal, W., P. L. Whitehouse, and E. J. O. Schrama (2015), Effect of GIA models with 3D composite mantle viscosity on GRACE mass balance estimates for Antarctica, *Earth Planet. Sci. Lett.*, *414*, 134–143, doi:10.1016/j.epsl.2015.01.001.
Veeraswamy, K., and U. Raval (2005), Remobilization of the palaeoconvergent corridors hidden under the Deccan trap cover and some major stable continental region earthquakes, *Curr. Sci.*, *89*(3), 522–530.
Vijay Kumar, T., S. Jagadeesh, and S. Rai (2012), Crustal structure beneath the Archean Proterozoic terrain of north India from receiver function modeling, *J. Asian Earth Sci.*, *58*, 108–118, doi:10.1016/j.jseaes.2012.06.015.
Vita-Finzi, C. (2004), Buckle-controlled seismogenic faulting in peninsular India, *Quat. Sci. Rev.*, *23*(23-24), 2405–2412, doi:10.1016/j.quascirev.2004.01.008.
Vogt, P. R. (1971), Asthenosphere motion recorded by the ocean floor south of Iceland, *Earth Planet. Sci. Lett.*, *13*(1), 153–160, doi:10.1016/0012-821X(71)90118-X.
von Blanckenburg, F. (2004), Cosmogenic nuclide evidence for low weathering and denudation in the wet, tropical highlands of Sri Lanka, *J. Geophys. Res.*, *109*, F03008, doi:10.1029/2003JF000049.
Wandrey, C. J., and B. E. Law (1997), Maps showing geology, oil and gas fields and geologic provinces of South Asia, *U.S. Geol. Surv. Open File Rep.*, *97-470*(C), 1–16.
Wang, P., S. Clemens, L. Beaufort, P. Braconnot, G. Ganssen, Z. Jian, P. Kershaw, and M. Sarnthein (2005), Evolution and variability of the Asian monsoon system: State of the art and outstanding issues, *Quat. Sci. Rev.*, *24*(5-6), 595–629, doi:10.1016/j.quascirev.2004.10.002.
Watts, A. B. (2001), *Isostasy and Flexure of the Lithosphere*, Cambridge Univ. Press, Cambridge.
Watts, A. B., and K. Cox (1989), The Deccan Traps: An interpretation in terms of progressive lithospheric flexure in response to a migrating load, *Earth Planet. Sci. Lett.*, *93*(1), 85–97.
Weismüller, J., B. Gmeiner, S. Ghelichkhan, M. Huber, L. John, B. Wohlmuth, U. Rüde, and H. P. Bunge (2015), Fast asthenosphere motion in high-resolution global mantle flow models, *Geophys. Res. Lett.*, *42*, 7429–7435, doi:10.1002/2015GL063727.
Weissel, J. K., and M. A. Seidl (1998), Inland propagation of erosional escarpments and river profile evolution across the southeast Australian passive continental margin, in *Rivers Over Rock: Fluvial Processes in Bedrock Channels, Geophys. Monogr. Ser.*, vol. 107, edited by K. J. Tinkler and E. E. Wohl, pp. 189–206, AGU, Washington, D. C., doi:10.1029/GM107p0189.
Whipple, K. X. (2002), Implications of sediment-flux-dependent river incision models for landscape evolution, *J. Geophys. Res.*, *107*(B2), 2039, doi:10.1029/2000JB000044.
Whipple, K. X. (2009), The influence of climate on the tectonic evolution of mountain belts, *Nat. Geosci.*, *2*(2), 97–104, doi:10.1038/ngeo413.
Whipple, K. X., and G. E. Tucker (1999), Dynamics of the stream-power river incision model: Implications for height limits of mountain ranges, landscape response timescales, and research needs, *J. Geophys. Res.*, *104*(B8), 17,661–17,674, doi:10.1029/1999JB900120.
White, R., and D. McKenzie (1989), Magmatism at rift zones: The generation of volcanic continental margins, *J. Geophys. Res.*, *94*(B6), 7685–7729.
Whiting, B. M., G. D. Karner, and N. W. Driscoll (1994), Flexural and stratigraphic development of the west Indian continental margin, *J. Geophys. Res.*, *99*(94), 13,791–13,811, doi:10.1029/94JB00502.
Whittaker, A. C., and S. J. Boulton (2012), Tectonic and climatic controls on knickpoint retreat rates and landscape response times, *J. Geophys. Res.*, *117*, F02024, doi:10.1029/2011JF002157.
Whittaker, A. C., P. A. Cowie, M. Attal, G. E. Tucker, and G. P. Roberts (2007), Contrasting transient and steady-state rivers crossing active normal faults: New field observations from the Central Apennines, Italy, *Basin Res.*, *19*(4), 529–556, doi:10.1111/j.1365-2117.2007.00337.x.
Whittaker, J. M., A. Goncharov, S. E. Williams, R. D. Müller, and G. Leitchenkov (2013), Global sediment thickness data set updated for the Australian-Antarctic Southern Ocean, *Geochem. Geophys. Geosyst.*, *14*, 3297–3305, doi:10.1002/ggge.20181.
Widdowson, M. (1997), Palaeosurfaces: Recognition, reconstruction and palaeoenvironmental interpretation, *Geol. Soc. Spec. Publ.*, *120*(1), 1–328, doi:10.1017/CBO9781107415324.004.
Widdowson, M., and K. Cox (1996), Uplift and erosional history of the Deccan Traps, India: Evidence from laterites and drainage patterns of the Western Ghats and Konkan Coast, *Earth Planet. Sci. Lett.*, *137*(1–4), 57–69, doi:10.1016/0012-821X(95)00211-T.
Widdowson, M., and C. Mitchell (1999), Large-scale stratigraphical, structural and geomorphological constraints for earthquakes in the Southern Deccan Traps, India: The case for denudationally-driven seismicity, *Mem. Geol. Soc. India*, *43*(1), 425–452.
Willett, S. D., S. W. McCoy, J. T. Perron, L. Goren, and C.-Y. Chen (2014), Dynamic reorganization of river basins, *Science*, *343*(6175), 1248,765, doi:10.1126/science.1248765.
Wilson, J. W. P., G. G. Roberts, M. J. Hoggard, and N. J. White (2014), Cenozoic epeirogeny of the Arabian Peninsula from drainage modeling, *Geochem. Geophys. Geosyst.*, *15*, 3723–3761, doi:10.1002/2014GC005283.
Winterbourne, J., N. White, and A. Crosby (2014), Accurate measurements of residual topography from the oceanic realm, *Tectonics*, *33*, 982–1015, doi:10.1002/2013TC003372.
Wolf, R. A., K. A. Farley, and L. T. Silver (1996), Helium diffusion and low temperature thermochronometry of apatite, *Geochim. Cosmochim. Acta*, *60*(21), 4231–4240, doi:10.1016/S0016-7037(96)00192-5.
Woodroffe, S. A., and B. P. Horton (2005), Holocene sea-level changes in the Indo-Pacific, *J. Asian Earth Sci.*, *25*(1), 29–43.
Yamato, P., L. Husson, T. W. Becker, and K. Pedoja (2013), Passive margins getting squeezed in the mantle convection vice, *Tectonics*, *32*, 1559–1570, doi:10.1002/2013TC003375.
Zeitler, P. K., A. L. Herczeg, I. McDougall, and M. Honda (1987), U-Th-He dating of apatite: A potential thermochronometer, *Geochim. Cosmochim. Acta*, *51*(10), 2865–2868, doi:10.1016/0016-7037(87)90164-5.